HARD X-RAY CHARACTERISTICS OF SOLAR FLARES USING ELECTRON MONTE-CARLO CALCULATIONS AND BEAMED THICK TARGET MODEL

R. R. RAUSARIA*

Indian Institute of Astrophysics, Kodaikanal, India

(Received 27 September, 1991)

Abstract. The experimental results of X-ray bursts with spectral characteristics, spatial distribution, fast time variations, polarization, and directivity measurements carried out with Intercosmos, PVO/ISEE-3 spacecrafts, imaging instrument observations of Hard X-ray (HXIS) and Hard X-ray Burst Spectrometers (HXRBS) during solar maximum mission have been reviewed. The observed results about the above characteristics are discussed in detail in terms of non-thermal and thermal models. It is shown that the results can be interpreted in terms of beamed thick-target model in which electrons stream down to the loop footpoints and produce hard X-rays through electron-ion bremsstrahlung.

1. Introduction

Solar flares are explosions in magnetized plasma, accompanied by the release of roughly 10^{32} ergs of energy in a short interval of less than a second. This high release of energy manifests itself partly in the form of corpuscular radiation in which particles accelerated to energies in the MeV range have also been detected (Švestka, 1976). The precise nature of the acceleration mechanisms at work even today are speculative. Of the complete electromagnetic spectrum emitted during a flare, the study and analysis of the hard X-ray provides a powerful tool for the study of various parameters characterizing the incident beam of high-energy electrons. Solar hard X-radiation with photon energies greater than 10 keV is produced in observable intensity only during a flare and show rapid changes of intensity on time-scales of the order of ms to several minutes. The experimental characteristics of hard X-rays have been reviewed recently by Dennis (1985, 1988) or Tanaka (1987). Theoretical aspect of hard X-ray characteristics have been reviewed by Brown (1975), Haug (1979), and Brown and Smith (1981). However, there is no review on the topic concerning electron Monte-Carlo calculations. Therefore, in this paper we have taken a comprehensive look on the characteristics of hard X-rays with energies ≥ 10 keV using our own electron Monte-Carlo calculations.

The X-ray energy spectrum above 10 keV is in most cases consistent with a power law of the differential photon flux (Kane and Anderson, 1970). The photon spectral index takes values between 2 (hard spectrum) and 8 (soft spectrum). Most frequent spectral indices are around 4 to 5 whereas very hard radiation with spectral index < 3 is extremely rare. Above some critical energy ~ 100 keV the spectrum steepens rapidly, i.e., the spectral index increases (Kane and Anderson, 1970). This may be expressed

* On leave of absence from Regional Engineering College, Srinagar, India.

Astrophysics and Space Science **194**: 261–301, 1992.

by an additional cut-off factor of power-law form. In some events the power law extends to several hundreds of keV (Suri *et al.*, 1975).

The hard X-radiation is believed to be mainly due to bremsstrahlung in collisions between energetic electrons and the ions of the solar atmosphere. Electrons with power-law energy spectrum can produce power-law photon spectrum usually observed and, therefore, this fact was regarded as an evidence of the non-thermal origin of the solar hard X-rays (Takakura, 1966; Holt and Cline, 1968; Holt and Ramaty, 1969). The steepening of flare X-ray spectrum can be obtained in principle on a thermal basis assuming a mixture of plasma components at different temperatures (Chubb, 1970; Kahler, 1975; Brown *et al.*, 1979). However, a thermal interpretation is contradicted by the fact that, at very high temperatures needed to explain the slope of the X-ray spectrum, the thermal relaxation time is much higher than the X-ray burst duration. In addition, Lin *et al.* (1982) have directly observed the electron spectrum, escaping out of the solar atmosphere. This spectrum shows a constant spectral index in the energy ranges from 50 keV up to 10 MeV. These extremely high electron energies and the spectral shape cannot be explained on a thermal basis. Whereas the low-energy electrons are believed to be more or less thermal for high-energy electrons, non-thermal interpretation seems necessary.

The spatial distributions of hard X-ray sources during flares have been determined extensively by imaging instruments on SMM satellite (Van Beek *et al.*, 1980; Hoyng *et al.*, 1981) and on the HINOTORI spacecraft (Tsuneta *et al.*, 1984). With the aid of instruments on SMM it was possible for the first time to investigate the location and spatial extension of hard X-ray sources with a resolution of 8″ corresponding to 6000 km on the solar surface. The analysis of Hard X-ray Imaging Instrument (HXIS) on SMM in the energy range 16–30 keV revealed that, in several flares, some of the hard X-rays occurred as bright points. These bright points were synchronous and co-spatial with Hα and UV emissions (Hoyng *et al.*, 1981; Duijveman *et al.*, 1982). On the basis of synchronism of hard X-ray with Hα and UV, these authors proposed beamed thick-target model for the hard X-ray and chromospheric footpoints emissions. Further studies of chromospheric response to electron beam hypothesis have been found to be consistent with beamed thick-target model (Acton *et al.*, 1982; Canfield *et al.*, 1984; Fisher *et al.*, 1984). More thorough analysis of HXIS data has been carried out by MacKinnon *et al.* (1985). MacKinnon *et al.* have also correlated the HXIS results with HXRBS. They found that footpoint photon fluxes are much less than expected from HXRBS extrapolation, casting doubt on conventional thick-target beam interpretation for X-ray generation. Simultaneous X-ray images in hard (20–40 keV) and softer (6.5–15 keV) energy ranges have also been obtained with the hard X-ray telescope aboard the HINOTORI satellite (Takakura *et al.*, 1986; Tsuneta *et al.*, 1984). The HINOTORI observations show that some hard X-ray image ($\sim$ 20 keV) are consistent with electron beam precipitations to the footpoint (Tsuneta *et al.*, 1983). However, in some cases the hard X-ray characteristics different from the above-quoted have been found (Tsuneta *et al.*, 1984).

The vertical structure of a hard X-ray source can also be obtained from observations

with two or more satellites separated in heliographic longitude (Catalano and Van Allen, 1973). Such multispacecraft observations can also make important contributions to the investigation of X-ray anisotropy. Solar X-ray bursts have been observed simultaneously by detectors aboard the international Sun–Earth Explorer-3 (ISEE-3) and the Pioneer–Venus–Orbiter (PVO). A rare set of circumstances on 5 November, 1979 permitted valuable measurements of spatial structure of ≥ 100 keV X-ray source in solar flares by PVO/ISEE-3 (Kane *et al.*, 1982). While the ISEE-3 spacecraft was at its normal location close to the Sun–Earth line, the PVO spacecraft was located 135° east of the Sun–Earth line. During a period of about 6 hr, three successive flares occurred in Hale Plage Region 16413, located at S 14°, E 45°. All these flares were in full view of the PVO instruments. The second flare was partially occulted by the photosphere from the PVO line of sight. Views angles of the two instruments on ISEE-3 and PVO were 51°.6, 47°.8 and 47°.7 and 90°.0, 94°.3 and 94°.8, respectively. These observations show that the hard X-ray source is located at altitudes of 2500 km (Kane *et al.*, 1982). The X-ray flux ratio from the PVO/ISEE-3 has been obtained by Kane *et al.* (1982) for the three flares on 5 November, 1979 in the energy range 100–200 keV and plotted against the minimum altitude $h'_{\min}$ of the X-ray source that would be observed from the PVO location. As reported by Kane *et al.* (1982), the flux ratio 'r' decreases rapidly with the increase in minimum observable altitude $h'_{\min}$ the decrease being 50% for $h_{\min} \simeq 2000$ km and 90% for $h_{\min} \simeq 2500$ km. By assuming the altitude structure of the 100 keV X-ray source in the three flares to be roughly similar, Kane *et al.* (1982) interpreted this decrease as the altitude dependence of the X-ray source brightness. The difference in the X-ray flux observed has been explained by Kane *et al.* (1982) in terms of partial occultation of the X-ray source by the photosphere from the PVO line of sight. Later, the directivity measurements was extended up to 1 MeV photon energy (Kane *et al.*, 1988). Brown *et al.* (1981, 1983) have shown that the height-structure observations can be explained in terms of a thick-target beam model. However, in their calculations the effect of source directivity was not taken into account. Also, the electron distribution was taken to be of power-law form, and dispersion in energy distribution about the mean is not included. Rieger *et al.* (1983) and Vestrand *et al.* (1987) have also studied the variation of directivity of > 300 keV photons. Recently, Petrosian (1985) and Dermer and Ramaty (1986) have extended these calculations to relativistic electrons with energies > 10 MeV.

The mean free path of an electron incident either at 0° (small angle) or at 60° (large angle) is the same. However, the vertical distance traversed by the electron coming at 60° will be less than that coming at 0° (secant correction). As a result of this the electrons at 0° penetrate deeper into the chromosphere before getting stopped as compared to those electrons which are incident at larger angles (say 60°). The flux of bremsstrahlung which depends on the density of protons will, therefore, be more for 0° electrons that that for 60° electrons. The ratio of X-ray fluxes for 60°/0° will, therefore, be a decreasing function of height. Later we will show that by the inclusion of source directivity the results of the thick-target model correspond well with the observations. However, the spectrum is not the only criteria on which to decide between a thermal or a non-thermal interpretation.

The spatial measurements do not provide much insight into the acceleration mechanism of electrons responsible for the generation of hard X-rays. The acceleration mechanism can, however, be studied with the help of rapid time fluctuations of hard X-ray bursts. The most recent observations (Kiplinger *et al.*, 1983a; Hurley *et al.*, 1983; Kane *et al.*, 1983) show millisecond time variations in hard X-ray during flares. Besides the pulsating nature of these hard X-ray bursts with several peaks have also been reported (Kiplinger *et al.*, 1983b, 1984).

Lu and Petrosian (1988) have solved Fokker–Planck equations analytically and have carried out detailed and thorough study of time variations of X-rays. Emslie (1983) has also put forward the explanation of millisecond time structure in terms of non-thermal thick-target bremsstrahlung mechanism. In this model the electrons are injected downwards into the solar atmosphere from the acceleration point high in the corona. As they spiral about the guiding magnetic field lines, their energies and pitch angles are changed continuously by collisions with ambient particles. More thorough calculations for different atmospheric models has been carried out by Craig *et al.* (1985). Emslie (1983) has assumed that all the electrons are centered at mean energy and mean angle with delta-function distributions. But all the electrons will not have the same energy and angles and there will be a distribution of energy and angles at a given column density (Haug *et al.*, 1985; Leach and Petrosian, 1981). The observations of Kiplinger *et al.* (1983b) and Kane *et al.* (1983) reveal a harder spectra at the peaks of the X-ray pulse compared to that at the valleys. This aspect has also been considered by Emslie (1983). However, these calculations do not show the effect of the distribution in the electron incidence angle on the X-ray spectra with column density.

Quantitative information about the velocity distribution function of electrons could be derived from the measurements of the directivity and polarization of the hard X-rays. Earlier indirect measurements of the directivity of hard X-rays above 15 keV were carried out by various works by studying the centre-to-limb variation of the frequency of occurrence of hard X-ray bursts (Ohki, 1969; Pinter, 1969). The best study of centre-to-limb variations of the hard X-ray burst occurrence do not show any significant longitudinal dependence (Kane, 1974; Datlowe *et al.*, 1977). More recent work by Vestrand *et al.* (1987) shows evidence for directivity from centre-to-limb for photon energies > 300 keV. The direct measurements of the directivity using the spacecrafts separated in heliocentric orbit has been carried out by Kane *et al.* (1988). The earlier measurements of the directivity were for photon energies in the range 50–200 keV and were later extended up to 1 MeV. The observations are consistent with isotropic model and disagree with theoretical predictions of Vestrand *et al.* (1987). Calculations by Koul *et al.* (1987) show that if the spacecrafts are separated in longitude by more than 60° then there should be observable anisotropy of hard X-rays.

If the angular distribution of the high-energy electrons is anisotropic, this is most directly inferred from the polarization properties of the X-radiation emitted by them as bremsstrahlung. The X-ray spectrum and the degree of polarization is dependent on the energy and angular distribution of the fast electrons which, in turn, is strongly affected by the propagation characteristics of the electrons in the ambient atmosphere. The

potential importance of X-ray polarization as diagnostics of energetic flare electrons has been discussed by Korchak (1967), Elwert (1968), Elwert and Haug (1970), Haug (1972), Brown (1972), Langer and Petrosian (1977), and Leach and Petrosian (1983). In the investigation by Elwert and Haug (1970) the calculation of X-ray polarization was based on electron energy distributions inferred from observed X-ray spectra, using the total bremsstrahlung cross-section. They employed *ad hoc* angular distributions of the form $\sin^2 \alpha$. Haug (1972) extended this work to relativistic energies assuming power laws for the instantaneous electron spectra in the interaction region; his angular distributions were again independent of electron energy. Brown (1972) included the effect of electron scattering and energy loss in a thick target on the X-ray polarization. In this calculation, however, the dispersion in energy and angular distribution about the mean value was not taken into account. The effect of photospheric back-scattering on the X-ray polarization has been studied by Henoux (1975), Langer and Petrosian (1977), and Bai and Ramaty (1978); generally, it results in a reduced degree of polarization. Emslie and Brown (1980) have evaluated the polarization of X-rays in terms of a thermal model characterized by the appearance of two collisionless conduction fronts. The resulting degree of polarization is of the order of a few percent.

By solving a time-independent Fokker–Planck equation, Leach and Petrosian (1981) have investigated the variations of the energy and pitch-angle distributions of high-energy electrons injected into a cold hydrogen plasma containing either an open or closed magnetic field structure. Their results were used to calculate the spectra, directivity, and polarization of the X-radiation produced as bremsstrahlung by these electrons (Leach and Petrosian, 1983; hereafter referred to as LP).

The measurement of X-ray polarization is highly difficult, and there exists only few observations (Tindo *et al.*, 1970, 1972a, b, 1976; Nakada *et al.*, 1979; Tramiel *et al.*, 1984). They show that the X-rays may be considerably polarized during strong flares, whereas in the most recent observations (Tramiel *et al.*, 1984) no statistically significant polarizations was detected during 6 relatively weak X-ray flares. So the experimental results are still inconclusive.

In the present work we employ the fully relativistic Monte-Carlo calculations on multiple scattering of non-thermal electrons with initial energy E_0 (Haug *et al.*, 1985) which allow to study the effect of dispersion in energy and angular distribution of fast electrons. If we use these distributions we present the results of our analysis on the spectrum, directivity, polarization, and fast time variation of X-rays. We also seek an explanation for the flux ratio observed by Kane *et al.* (1980b, 1982). Before we proceed to the calculations of spectrum, directivity, and polarization of the X-rays, it is desirable to give general features of calculating the electron distributions taking dispersions into account and also present the formalism used to calculate the X-ray flux.

2. Electron Distributions

Usually, the energy specrum of the non-thermal electrons is deduced from the measured X-ray spectra and the electron energy spectrum above 10 keV is taken to be power law

in form. Here we consider initially monoenergetic incident beams of electrons having energies of 60, 100, 300, and 500 keV, characterized by a velocity vector **v**. The choice of monoenergetic beams is justified by the fact that the power-law shape of the distribution can be obtained by giving suitable weights to monoenergetic electrons. Furthermore, due to collisions the electron beam broadens at higher column densities and becomes a continuous distribution almost independent of the original degree of beaming at injection. However, at lower columns densities near the acceleration site electron distributions are dependent on the original degree of beaming. The components of **v** in a coordinate system with z-axis are $\sin\alpha\cos\phi$, $\sin\alpha\cos\phi$, $\sin\alpha\sin\phi$, and $\cos\alpha$, where α is the incidence angle with respect to the vertical direction and becomes the pitch angle in the presence of a magnetic field. We consider the electrons directed towards the chromosphere from the acceleration site situated in the corona at 0°, 30°, and 60° incidence angles. Electron transport has been calculated as a function of column density/height in the atmosphere.

We consider a fully-ionized thermal plasma consisting of protons and electrons. It is assumed that the relativistic electron beam will be influenced by Coulomb collisions between the beam electrons and the thermal protons and electrons. Since, for chromospheric and coronal plasma the mean free path, as determined by the minimum scattering angle, is only a fraction of centimeter, it is not possible to treat all the small-angle deflections in a pure Monte-Carlo procedure. The path of electrons is, therefore, divided into two parts: a condensed history of the small-angle scattering process treated analyti-

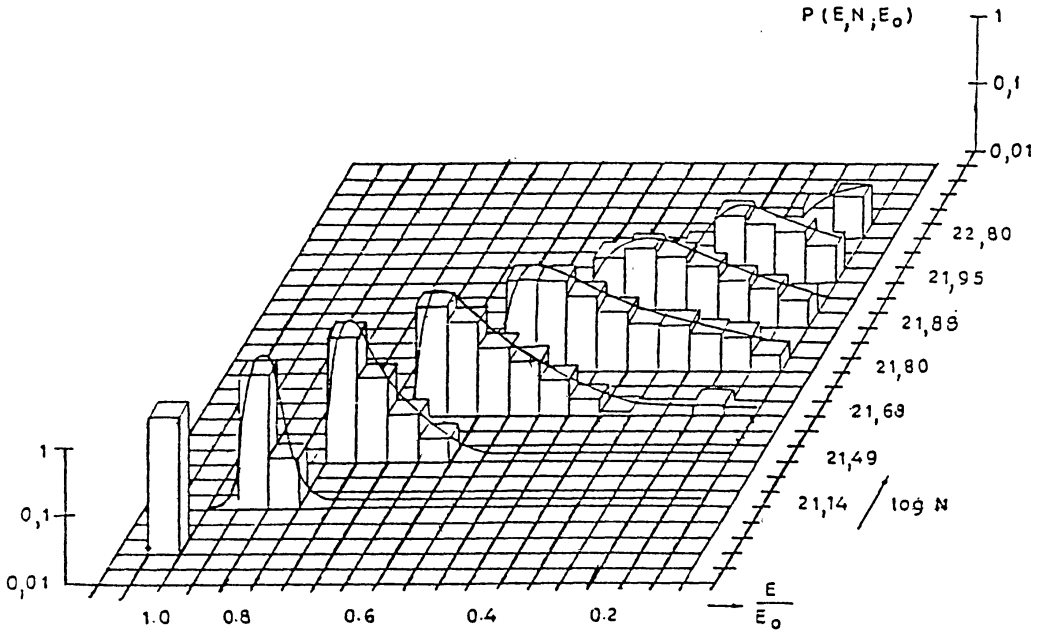

Fig. 1a. Variation of electron energy distribution with column density (No. of proton cm^{-2}). The initial electron energy is 300 keV incident at 0° (Haug *et al.*, 1985a).

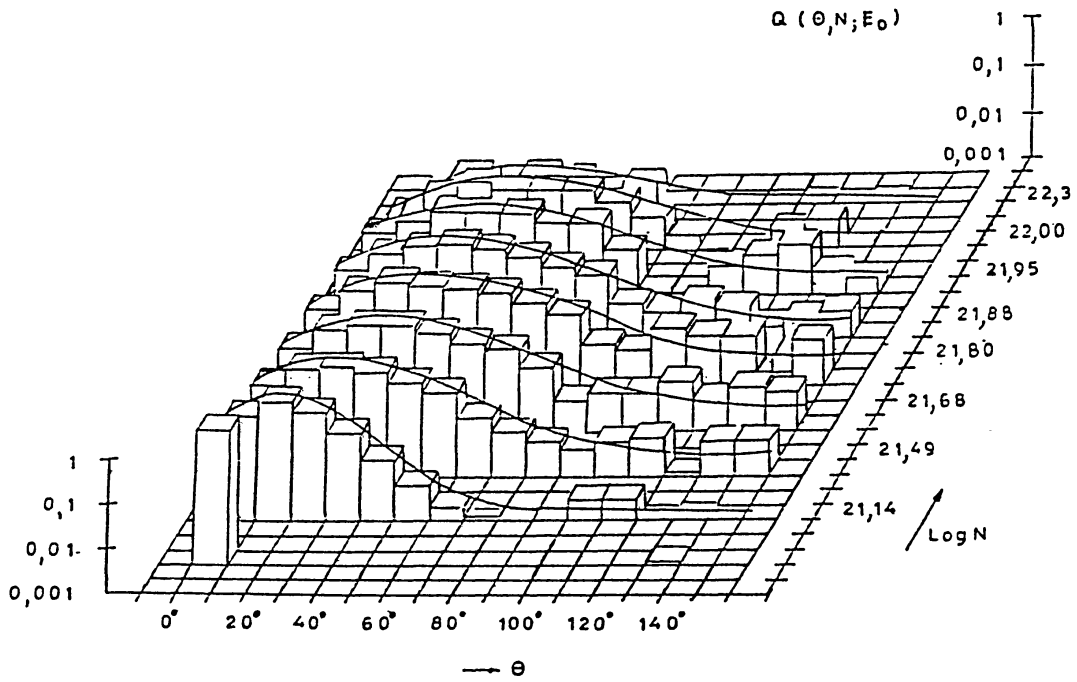

Fig. 1b. Variation of electron angular distribution with column density. The initial electron energy is 300 keV incident at 0° (Haug *et al.*, 1985a).

cally followed by Monte-Carlo calculations of a single large-angle collision process. Details of the calculations are given by Haug *et al.* (1985) and Koul *et al.* (1985).

We have considered electron starting at the location $S = 0$, which is taken as the acceleration site situated high up in the corona. The random walk of each electron is followed towards the chromosphere until it has lost nearly its total energy, i.e., $E < E_{\min}$, where $E_{\min}$ is $\frac{1}{20}$ of the initial energy E_0. It turned out that for all scale heights used, the results depend only on the column density $N(S) = \int_0^S n(S)\,\mathrm{d}s$, the member of protons cm^{-2} or electrons cm^{-2} within the column traversed. By this procedure we determine the electron energy and angular distributions at different heights (see Haug *et al.*, 1985; for details). The energy and angular distributions of electrons are shown in Figures 1(a), 1(b), and 2. The number of particles followed is between 1000–2000 and gives good statistics.

A similar procedure for the computation of the pitch angle and spatial distribution of energetic electrons including the effects of an ambient magnetic field has been employed by Bai (1982) who has neglected large angle scattering in his calculations. Our calculations show that width of the electron angular distributions are considerably modified due to inclusion of large angle scatterings. As a result of this, the widths of angular distributions obtained by our method are larger than those using the Bai method. Leach and Petrosian (1981) have used the time-independent Fokker–Planck equation to determine the variation of the energy and pitch-angle distribution of high-energy electrons injected into a cold hydrogen plasma containing either an open or closed

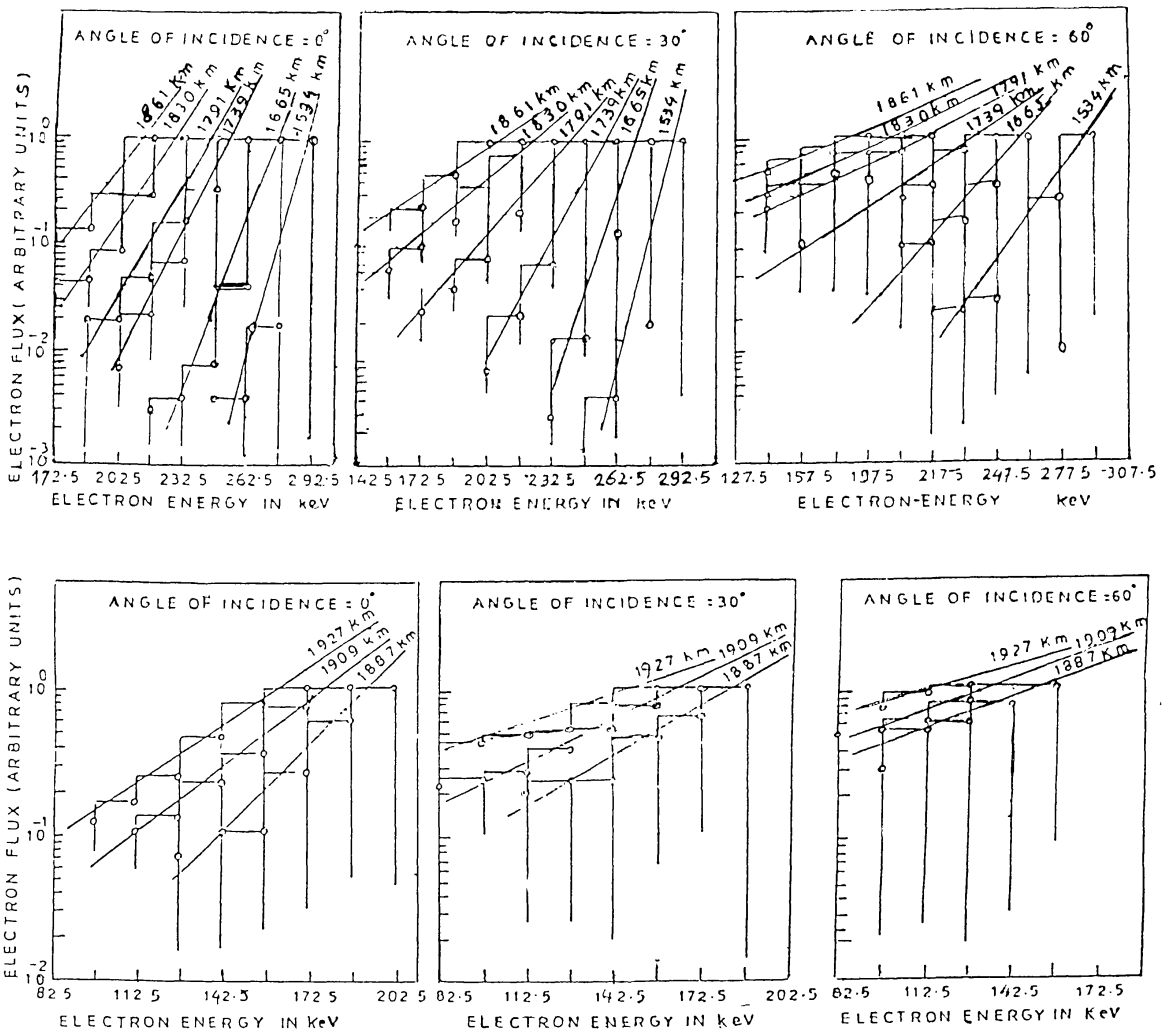

Fig. 2. Variation of electron spectral index with column density. The initial electron energy is 300 keV for incidence angles 0°, 30°, and 60° (Koul *et al.*, 1985).

magnetic field structure. In these investigation the injected electrons have a power-law spectrum.

3. Energy Spectra and Angular Distribution of X-Ray

The changes in the electron energy and angular distributions produce the corresponding change into X-ray energy spectrum and angular distribution. The photon flux produced by electrons in a fixed direction is given by

$$J(\vartheta) = n_{\mathrm{H}} \int_{1+k}^{\infty} \mathrm{d}\varepsilon \, \mathrm{d}(\cos\alpha) \int_{0}^{\pi} \mathrm{d}\phi \, g(\alpha) \, \frac{\mathrm{d}^2\sigma}{\mathrm{d}(\mathrm{h}\nu)\,\mathrm{d}\Omega} \, f(\varepsilon) v(\varepsilon)$$

$$(\text{photons cm}^{-2}\,\text{s}^{-1}\,\text{keV}^{-1}\,, \qquad (1)$$

where ε is the electron energy in units of its rest mass energy mc^2; $k = h\nu/mc^2$, the photon energy in the same unit; $d^2\sigma/d(h\nu)\,d\Omega$, the differential bremsstrahlung cross-section; $g(\alpha)$, the electron angular distribution; $f(\varepsilon)$, the electron energy distribution; $v(\varepsilon)$, the electron velocity; ϑ, the angle between the vertical direction and the line of sight; θ, the angle between the electron and photon directions.

In the presence of a magnetic field the electron direction will change continuously due to spiralling. The angle ϑ will depend on the incidence angle α, the angle θ, and on the azimuth angle ϕ of the electron relative to vertical direction (magnetic field) – i.e.,

$$\cos\vartheta = \cos\alpha\cos\theta + \sin\alpha\sin\theta\cos\phi\,. \tag{2}$$

For the differential cross-section the Born approximation following Sauter (1934) multiplied by the Coulomb correction (Elwert, 1939) is used in the present computation. It is given in Elwert and Haug (1971) as Equation (6). In this equation, the second term in parenthesis should read as $(\varepsilon^2 + 1 + \frac{1}{2}\varepsilon' p\cos\theta)$. Integrating over all the emission angles one get the bremsstrahlung flux as a function of energy only at different column densities (Koul *et al.*, 1985).

4. Temporal Analysis

The hard X-ray burst models mainly differ with regard to properties of electron injection (acceleration) mechanism and the nature of ambient plasma density. The high time resolutions provided by HXRBS on SMM require a detailed study of the evolution of non-thermal electron distributions as function of time. These observations have shown that the assumption, the collisional lifetime $t_c <$ injection time-scale is no longer valid (see, e.g., Emslie, 1983). To study the time variations of hard X-ray pulse, one need to carry out detailed time-dependent Monte-Carlo calculations. However, to get the idea of the effect of dispersion in electron energy and angular distributions on time profile, we follow a bit easier method of deducing the time variations for the spatial distributions. For non-relativistic electron energy Emslie (1983) has used the energy-loss formula

$$\frac{dE}{dt} = -\frac{2\pi e^4\Lambda}{E}\,nv\,, \tag{3}$$

where e (e.s.u.) is the electronic charge; n (cm^{-3}), the target density; Λ, the Coulomb logarithm; and $v = \sqrt{2E/m}$, the electron velocity. Equation (3) on integration yields

$$E^{3/2} = E_0^{3/2} - \frac{3K}{(2m_e)^{1/2}}\int_{t=t_0}^{t} n\,dt\,, \tag{4}$$

where $K = 2\pi e^4\Lambda$ and m_e is the electron mass. This equation is for non-relativistic energies.

In our calculations we have incorporated the relativistic effects to study the time variations. We follow the treatment given in Haug *et al.* (1985) to calculate the energy

loss by an electron while traversing a distance $\mathrm{d}l$ in a plasma of proton-electron density $n(l)$.

Our calculations are true for any part of the loop, but we want to emphasize the role of beamed thick-target model. Therefore, we have given more attention to the chromospheric part of the loop, since the density in the tenuous coronal part is approximately constant and dispersion in electron distribution especially for high energies is not significant. The density in the chromosphere rises sharply and electrons are stopped within a small column depth. We have divided the atmosphere into layers (labelled k) or column density interval ΔN_K. Their boundaries are chosen such that on the average, the energy of electron travelling perpendicularly to the layer is reduced by 5% of the initial energy E_0. The column densities N_{k-1} and N_k, respectively, at the layer boundaries are related to energies $E_K = (1 - K/20)E_0$ and the layer thickness is given by $\Delta N_K = N_k - N_{k-1}$. The mean column density $\overline{N}_k$ of the kth layer is defined by level S_k where the average electron energy is

$$\overline{E}_k = \tfrac{1}{2}(E_{k-1} + E_k)\,, \tag{5}$$

whenever an electron crosses the level S_k its energy E and angle θ is recorded and resultant electron distribution functions are calculated at each level S_k.

To calculate the time taken to traverse the kth layer of thickness ΔN_k, we may, therefore, approximate

$$\int_{t_{k-1}}^{t_k} \mathrm{d}t' = \int_{S_{k-1}}^{S_k} \frac{n\,\mathrm{d}l'}{\mathrm{d}l'/\mathrm{d}t}\,, \tag{6}$$

defining

$$\int_{t_{k-1}}^{t_k} n\,\mathrm{d}t' = \overline{n}_k(t_k - t_{k-1})\,,$$

where $\overline{n}_k$ is the mean density of the column traversed. As the electron traverses the denser layers there is continuous degradation in the electron energy resulting in a decrease in its velocity. The average velocity of the electron $\overline{V}_k = \overline{\mathrm{d}l'/\mathrm{d}t}|_K$ within a layer S_k is calculated by use of the relativistic formula

$$\frac{1}{\beta^2} = \frac{(E = mc^2)^2}{E(E + 2mc^2)}\,.$$

However, as discussed above there will be a distribution of electron energies crossing the layer S_k, so the average velocity is given by

$$\overline{V}_k = \frac{\int_v f(V, \theta, N_k; V_0)\,\mathrm{d}V}{\int f(V, \theta, N_k; V_0)\,\mathrm{d}V}\,.$$

Thus, we have in Equation (6)

$$\bar{n}_k(t_k - t_{k-1}) = \frac{\int_{s_{k-1}}^{s_k} n \, dl'}{\overline{V_k}}$$

or

$$t_k - t_{k-1} = \frac{N_k}{\bar{n}_k \overline{V_k}} \, .$$

Since we use the distribution function $f(V, \theta, N_k; V_0)$ to calculate the average velocity within the column traversed so the results include the dispersion effects. Equation (7) gives the time taken to traverse the layer S_k and following this method we have converted X-ray height profile into time profiles.

5. Results and their Relation to Observations

If we use the bremsstrahlung cross-section given in Elwert and Haug (1971) and the distribution function $f(\varepsilon)$ and $g(\alpha)$ described in Section 2, we have computed the energy spectra (Figures 3(a) and 3(b)) and angular distribution of X-rays (Figures 4(a) and 4(b)) for different column densities and photon energies. Figure 3(a) shows the energy spectrum at various depths in the solar atmosphere. Different curves have been obtained by integrating the photon flux over the emission angles. The figure clearly shows the variation in spectral index of the generated X-rays from the lower column density (reference column density, the column density at which the dispersion in electron energy and angular distribution is insignificant) of the atmosphere to the higher column density levels. As the beam of electrons injected at the top moves through the atmosphere, the number of low-energy electrons increase due to the attenuation of high-energy electron with the increase in column density. Thus the number of low-energy photons becomes larger resulting in the progressively steeper nature of X-ray spectra. However, no such observation showing the spatial dependence of spectral index with column density has been reported to-date. In Figure 3(b) we plot the energy spectra integrated over all the depths, i.e., we obtain a spatially integrated over all the depths, i.e., we obtain a spatially-integrated X-ray energy spectrum. The figure shows the variation of X-ray energy spectrum for three discrete angles of electron incidence. As is clear from the figure the spatially-integrated X-ray flux shows only a mild dependence on the electron incidence angles. We further note that the shape of calculated spatially-integrated spectrum corresponds well with the observed energy spectrum obtained from PVO and ISEE-3 spacecrafts (Figure 1 of Kane *et al.*, 1980).

Figure 4 depicts the evolution of X-ray flux with depth as a function of emission angle for different photon energies 10, 20, 50, 100, 150, and 200 keV. The incident electron

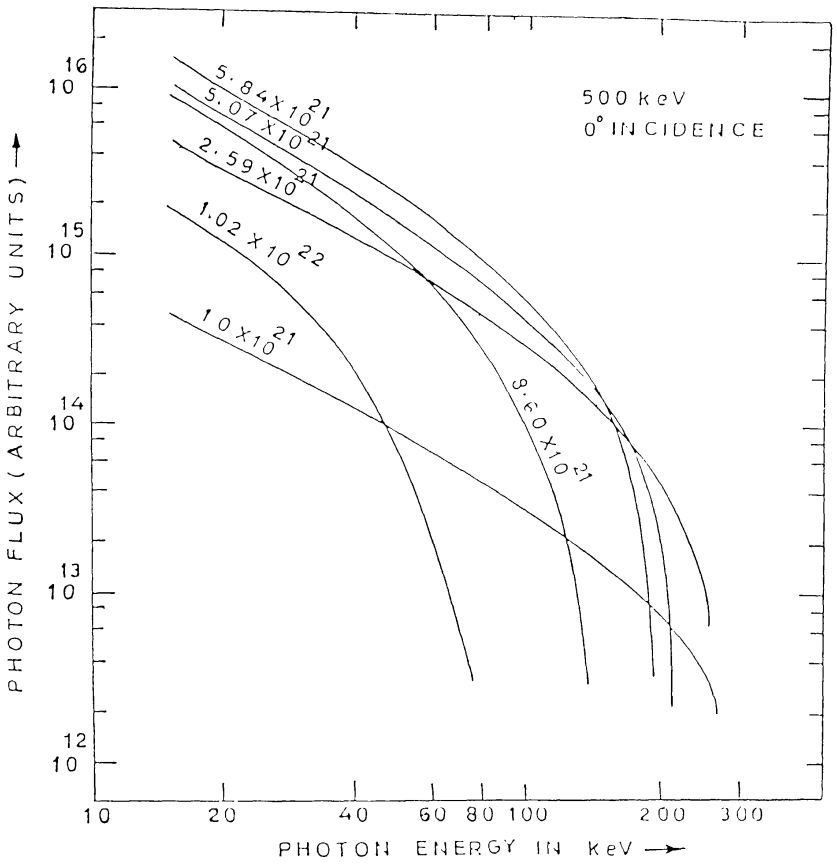

Fig. 3a. Energy spectra of X-rays at various column densities (No. of protons cm^{-2}) for a 300 keV electron beam incident at 0° (Koul *et al.*, 1987).

energy is 300 keV. The flux is highly anisotropic at lower column densities and high-energy photons show strong beaming in the forward direction, i.e., towards the photosphere. With increased column density the flux progressively tends towards isotropy. This figure also shows that isotropization is slower for higher energies compared to low-energy photons. Our calculations thus support the idea that electrons are initially produced as monoenergetic beams and give rise to power-law shape of hard X-ray spectrum during interaction process. The analysis of HXIS data by MacKinnon *et al.* (1985) show that footpoint pixels have softer spectra than intervening pixels which supports our calculations.

Figure 2 shows that electrons incident at 60° are stopped at greater heights (lower column density) than those incident at 0°. The mean free path of an electron incident at 0° (secant correction). As a result of this the electrons at 0° penetrate deeper into the chromosphere before getting stopped as compared to those electrons which are incident at larger angles (say 60°). The ratio of X-ray fluxes for 60°/0° will, therefore, decrease at lower altitudes. The ratios of the flux produced by 60° to 0° electron incidence for different photon energies are plotted in Figure 5. From the figure we find

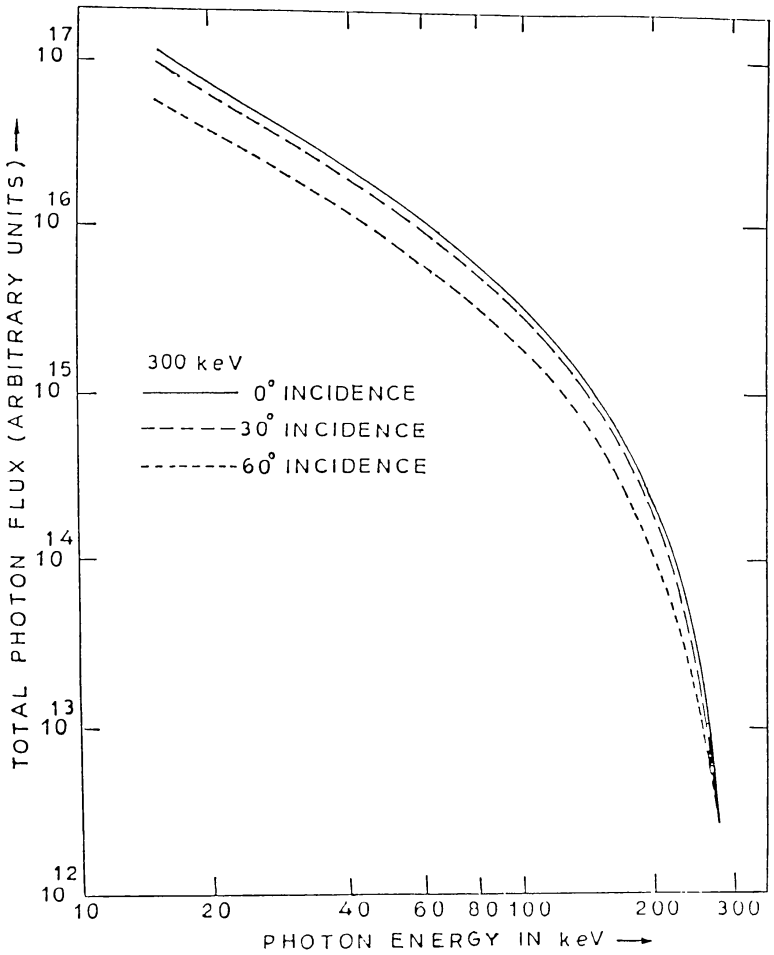

Fig. 3b. X-ray flux spectra integrated over all the column densities, i.e., spatially-integrated X-ray energy spectrum for a 300 keV electron beam incident at 0°, 30°, and 60° (Koul *et al.*, 1987).

that the nature of calculated curve resemble well with the measured curve of Kane *et al.* (1979). While accepting the explanation of the observed results put forward by Kane *et al.* (1982) in terms of photospheric absorption, we feel that the results could also be explained in terms of different incidence angles of electron beam together with attenuation at different depths in the solar atmosphere.

A measure of the anisotropy A is the quotient of J_1 for $\vartheta_1 = 90°$ (perpendicular to the electron incidence direction) to J_2 for $\vartheta_2 = 180°$ (opposite to the electron incidence). At higher column densities the X-ray distribution (Figures 4(a) and 4(b)) becomes more and more isotropic and the difference between fluxes at 90° and 180° become smaller. To illustrate this feature we have studied the variation of the anisotropy quotient A as a function of column density in Figures 6(a) and 6(b) for photon energies 10, 20, 50, 100, and 150 keV. The important feature to note in this figure is that the anisotropy quotients for higher photon energies 100 and 150 keV do not have the same trend as is found for lower energy 10, 20, 50 keV photons. To study the anisotropy quotient:

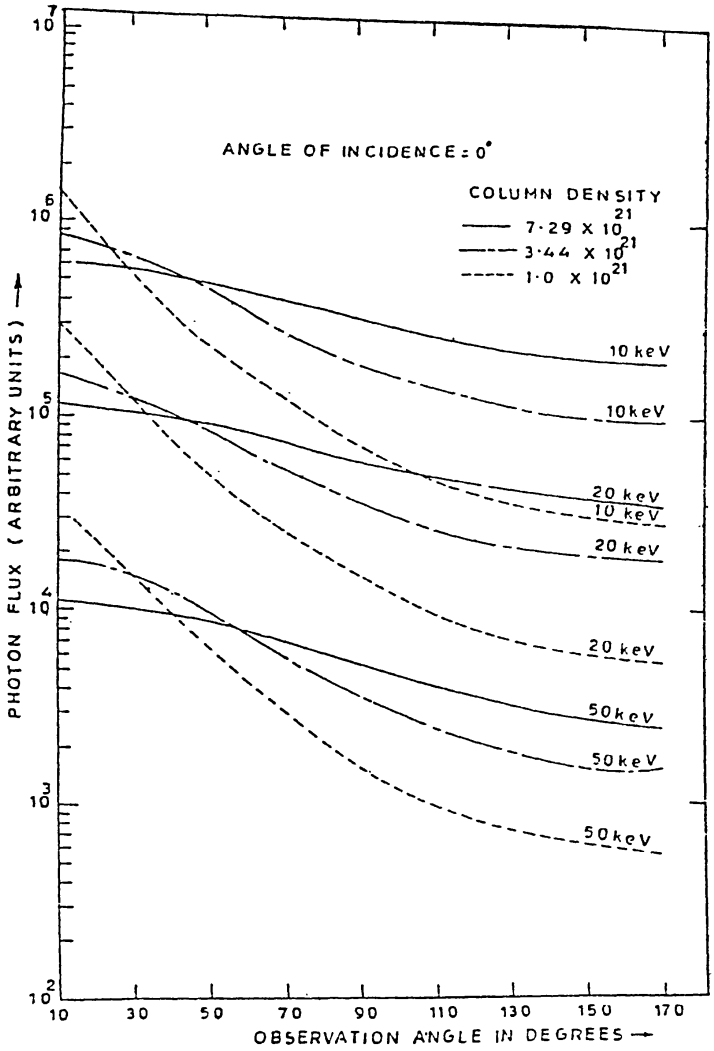

Fig. 4a. Variation of photon flux for photon energies 10, 20, and 30 keV as a function of the observation angle (the angle between magnetic field and direction of photon emission) at various column depth. The incident electron energy is 300 keV (Koul *et al.*, 1987).

(i) J_1 for $\vartheta_1 = 90°$ to J_2 for $\vartheta_2 = 150°$, i.e., the difference in observation/emission angle is 60°.

(ii) J_1 for $\vartheta_1 = 90°$ to J_2 for $\vartheta_2 = 130°$, i.e., the difference in observation angle/emission angle is 40°.

Comparisons of Figures 6(a) and 6(b) gives an opportunity not only to study the variation of A with column density but also the effect of changes in the observation angle on the anisotropy quotient. From the figures we note that for all the angles chosen, the nature of the curves remain the same. However, one can see that for the lower difference angle of 40° the quotient lies between 1 and 4 and it changes less with column density than it does for difference angles above 60° where the quotient is greater than four and the decrease with the column density becomes progressively larger. Thus, it can be

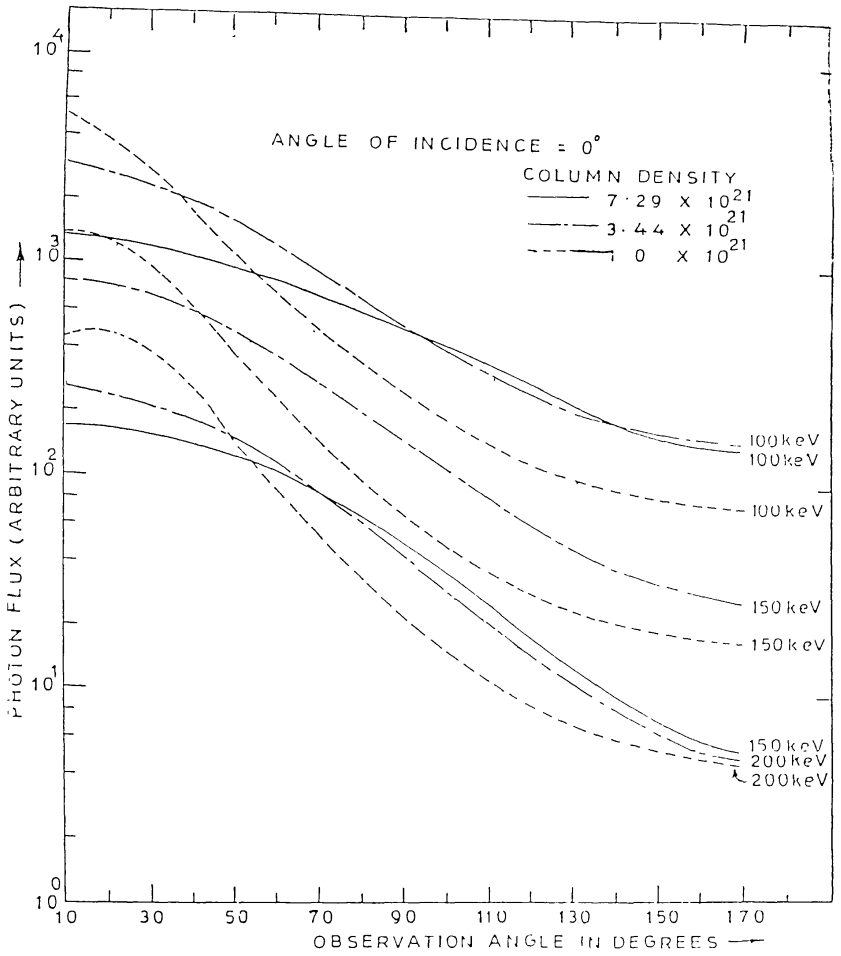

Fig. 4b. Variation of photon flux for photon energies 100, 150, and 200 keV as a function of the observation angle (angle between magnetic field and direction of photon emission) at various column depths (Koul *et al.*, 1987).

inferred that with the increase in difference angle, the anisotropy quotient A becomes higher and increases more rapidly towards higher column densities.

The directivity of 50–100 keV X-ray emissions from solar flares have been measured with instruments on the ISEE-3 and PVO spacecraft (Figure 2 of Kane *et al.*, 1980). These measurements have now been extended up to 1 MeV by Kane *et al.* (1988). The conclusions arrived by Kane *et al.* (1980) favours an isotropic model for X-ray generation. In five events observed by Kane *et al.* (1980) the difference in view angles of the two spacecrafts was less than 30°. In other three events the difference angle was more than 30° and in one case it was as large as 66°. In order to correlate these observations with our calculations we plot in Figure 7 the flux ratio of 50–150 keV photons as a function of difference angle (keeping either 90° (right-hand scale) or 180° (left-hand scale) emission angle fixed and vary the other angle) at a fixed column density where significant dispersion of the original electron beam has already taken place. From this figure we note that the flux ratio for 50–150 keV photons is almost the same up to the difference angle of about 50°, but with the increase in difference angle beyond 60° the

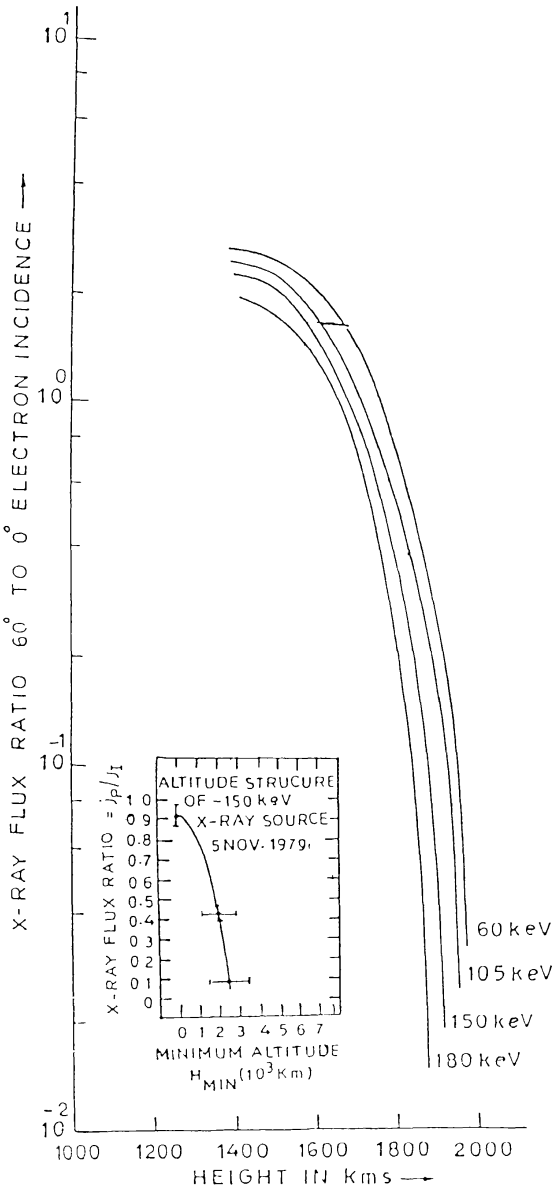

Fig. 5. Variation of X-ray flux ratio with height and its comparison with observations (Koul *et al.*, 1985).

flux variations become significant. Furthermore, for the difference angles less than 50° one would find an isotropic model, however, for the difference angles more than 60° one finds anisotropic model for X-ray generation. Our calculations do point towards an isotropic model for difference angles less than 60° as was observed by Kane *et al.* (1980). However, for difference angle greater than 60° one would expect anisotropy of the X-ray distributions.

The variations of photon flux as a function of column density (for 30, 45, 60, and 90 keV photons) are plotted in Figures 8(a) and 8(b). The X-ray production maximizes at different column densities for various electron energies incident at a fixed angle. Furthermore, we note that the photon production corresponding to each spot value of

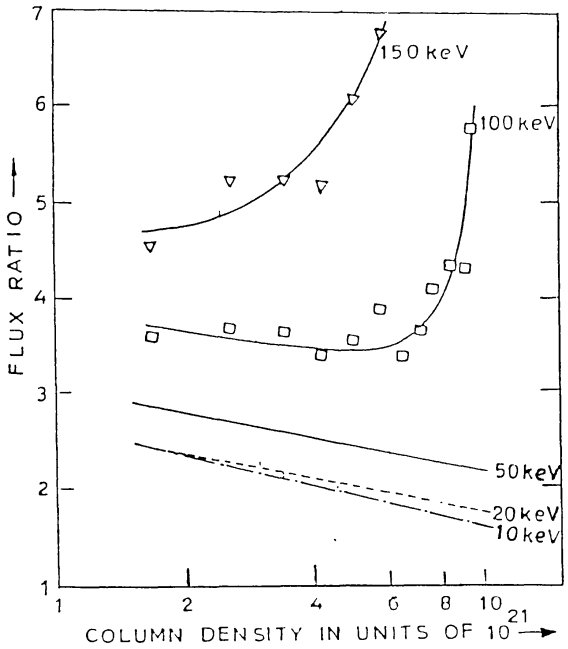

Fig. 6a. Variation of photon flux ratio or anisotropy quotient between J_1 for $\vartheta_1 = 90°$ (perpendicular to electron incidence) to J_1 for $\vartheta_2 = 180°$ (opposite) to electron incidence with column density (No. of protons cm^{-2}) for photon energies 10, 20, 50, 100, and 150 keV and the incident electron energy 300 keV (Koul *et al.*, 1987).

the energy maximizes at lower column density for 60° incidence compared to 30° and 0° electron incidences. The width of the height distribution for a particular photon energy becomes broader with the increase in electron incidence angle. For 60° electron

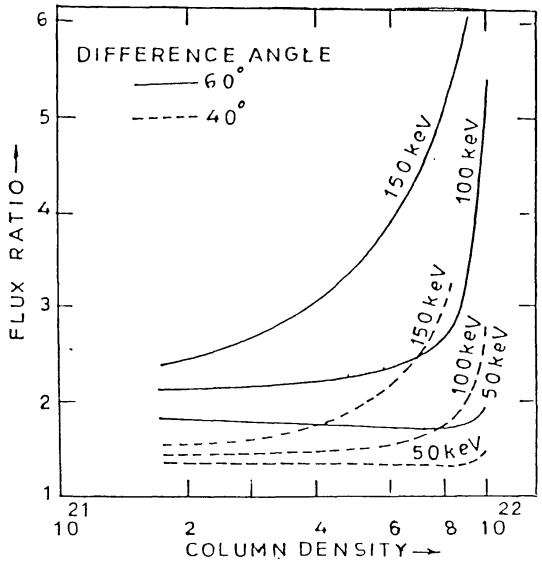

Fig. 6b. Same as Figure 6(a) but for angles $\vartheta_2 = 150°$ (solid curves) and $\vartheta_2 = 130°$ (dashed curves) for energies 50, 100, and 150 keV. The difference of angles are $\vartheta_2 - \vartheta_1$, i.e., 60° (solid curves) and 40° (dashed curves) (Koul *et al.*, 1987).

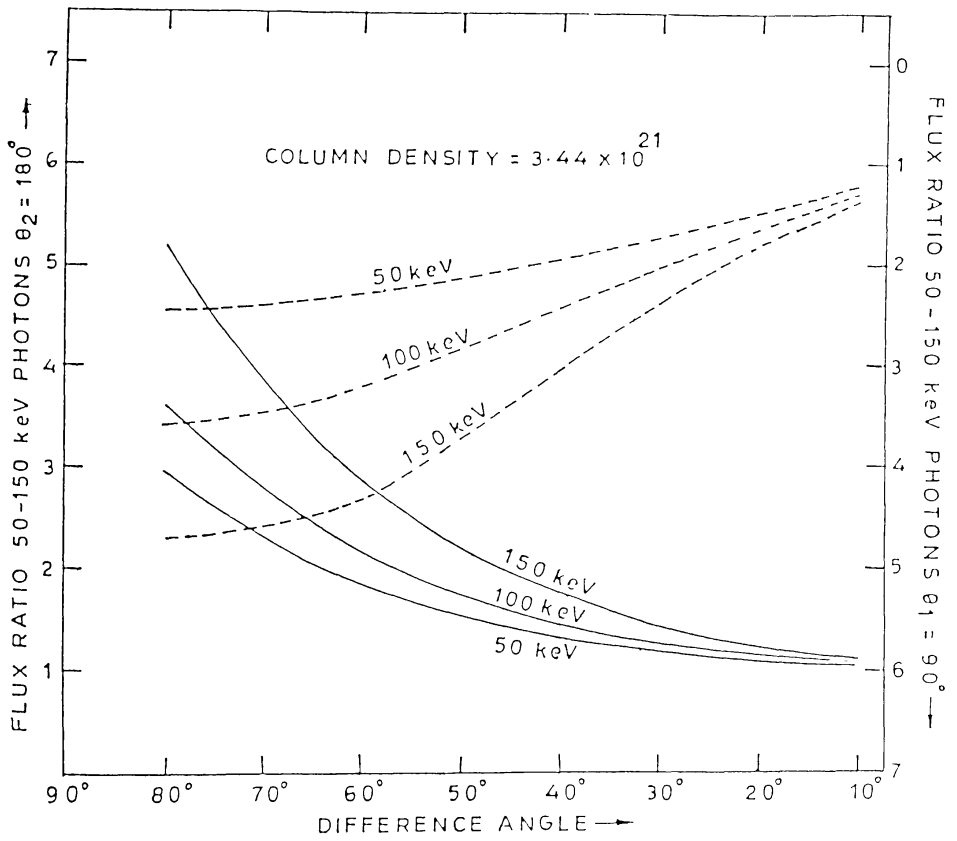

Fig. 7. Ratio of 50–150 keV X-ray fluxes for two different view angles ϑ_1 to ϑ_2 as a function of difference angles $\vartheta_2 - \vartheta_1$ at representative column density (No. of protons cm^{-2}) 3.44×10^{21}, for the left-hand vertical scale (-curves) $\vartheta_2 = 180°$ is fixed and ϑ_1 varies from 90° to 170° and for right-hand vertical scale (-curves) $\vartheta_1 = 90°$ is fixed and ϑ_2 varies from 100° to 170° (Koul *et al.*, 1987).

incidence the distribution of photon flux with height becomes broadened and does not show much pronounced peak. The width of the X-ray profile becomes smaller with increase in photon energy and for electron incidence angles approaching 0°.

Figure 9(a) depicts the evolution of X-ray flux as a function of time for photon energies 30, 45, 60, and 90 keV. In our calculations we have assumed the instantaneous injection of electrons. The figure shows that the curves for 30° and 60° are progressively wider than for 0°. The peak for high-energy photons appears earlier than that for low-energy photons. This is consistent with the observations of Kiplinger *et al.* (1983). We note in the figure that the width of the curves decreases with increase in photon energy. The width of each curve is characterized by the collisional lifetime of the electrons. The collisional lifetime of an electron is

$$t_c = \frac{(2m_e E^3)^{1/2}}{3k\bar{n}} .$$

This formula is valid for non-relativistic formulation. We have derived expression for t_c using relativistic formulation. The expression is complicated and similar terms appear.

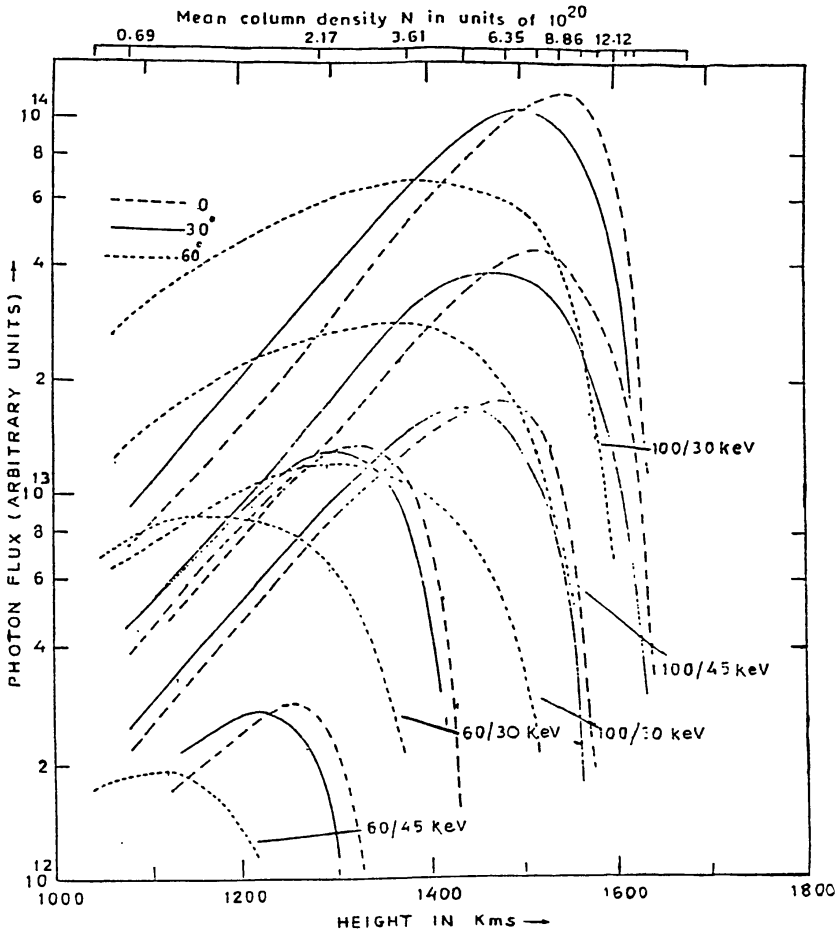

Fig. 8a. Variation of photon flux with height for 0°, 30°, and 60° electron incidence angles. The incidence electron energies are 60 and 100 keV. 100/30 keV on the curve signify 100 keV electrons and 30 keV photon energy (Koul *et al.*, 1988).

Therefore, for simplicity of interpretation we follow the non-relativistic formulation (Emslie, 1983). Since $\bar{n}$ is proportional to the stopping column density which, in turn, is proportional to E^2 (Equation (16) of Haug *et al.*, 1985), we find that the collisional lifetime is proportional to $E^{-1/2}$. Thus for high-energy electrons the collisional lifetime will be small. The column densities corresponding to Figure 8 lie in between 10^{20} and 10^{21} protons cm^{-2} or electrons cm^{-2}. In the light of above discussions we find that higher photon energies are characterized by smaller profile widths (see Table I). These curves also depict that the X-ray curve maximizes at some intermediate time t_c in each case.

For comparison of results with observations one has to bear in mind that the assumption of monoenergetic and monodirectional beams at acceleration site are highly idealized. However, the choice of monoenergetic beam is justified by the fact that the power-law shape of distribution can be obtained by giving suitable weights to the monoenergetic electrons. Furthermore, due to collision the electron beam broadens at

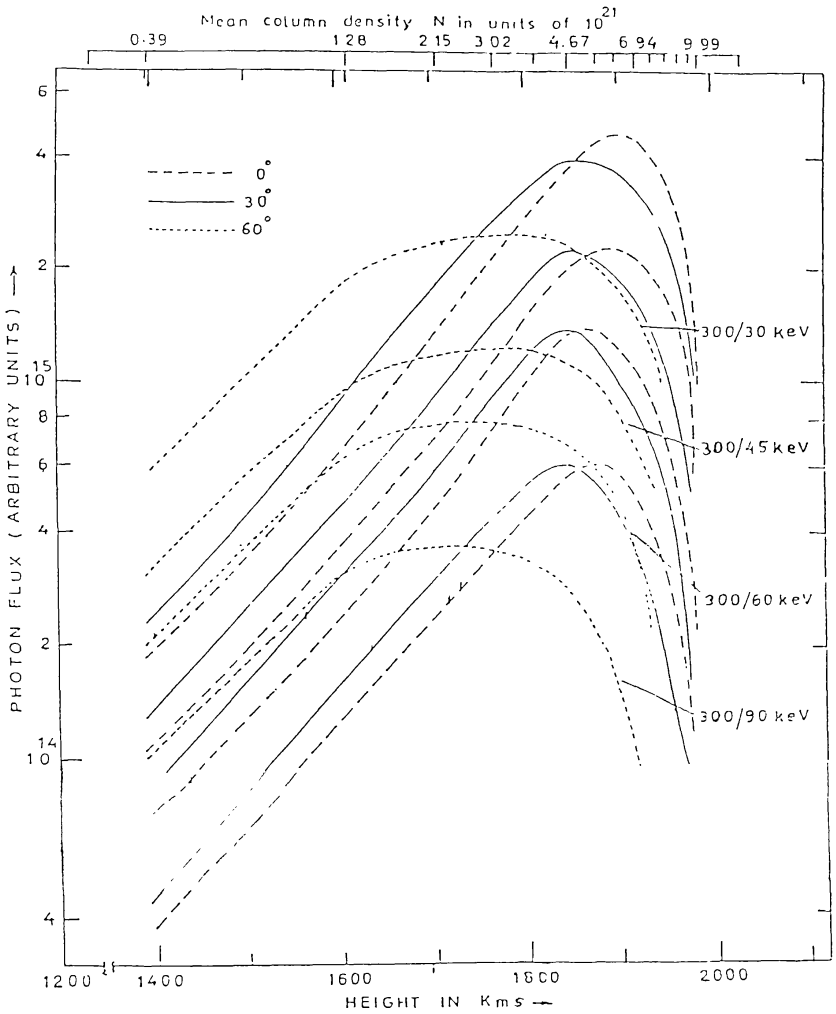

Fig. 8b. Same as Figure 1(a) but for the incident electron energies 300 keV (Koul *et al.*, 1988).

TABLE I

Full width at half maximum (s)

Electron energy	Angle of incidence	ε = 30 keV	ε = 45 keV	ε = 60 keV	ε = 90 keV	Total 15–285 keV
300 keV	0°	0.105	0.100	0.097	0.095	0.080
	30°	0.115	0.120	0.120	0.100	0.115
	60°	0.190	0.185	0.170	0.160	0.180
						5–100 keV
100 keV	0°	0.160	0.150	0.135	–	0.165
	30°	0.175	0.160	0.135	–	0.190
	60°	0.255	0.220	0.185	–	0.260

higher column densities and becomes a continuous distribution. We also find that the integrated X-ray emissions from the whole source has the character of the emission from a highly-broadened beam (Koul *et al.*, 1987). If we compare our results with those of Emslie (1983), we note that our results depend practically on the column density for all the scale heights used. Thus, to make t_c sufficiently small compared to observed lifetime of a hard X-ray burst we have to change N. A comparison of the results presented in Table I, to those of Emslie (1983) shows an increase in the X-ray pulse widths but in our case the widths are calculated at half the maximum instead of 10% of the maxima. With the increase in incidence angle we find that the width of the X-ray pulse increases and the increase is appreciable from 30° to 60° as compared to that from 0° to 30° as obtained by Emslie (1983) for various pitch angles.

It is very unlikely that the acceleration mechanism at work high up in the corona accelerates the electrons at discrete angles only. It, therefore, seems plausible to consider a wider angular distribution of electrons rather than a particular angle at start. Such angular distributions centered around 0°, may produce various peaks in the height profile of the X-rays. However, such peaks have not been observed in stereoscopic observations (Kane *et al.*, 1982; Hurley *et al.*, 1983). However, if there is a distribution of electron energies at the starting point, correspondingly there will be additional peaks present in the X-ray time profile.

Another possibility suggested by Kane *et al.* (1983) is that electrons are accelerated at a fixed angle and by the time they are absorbed in the solar atmosphere beam is

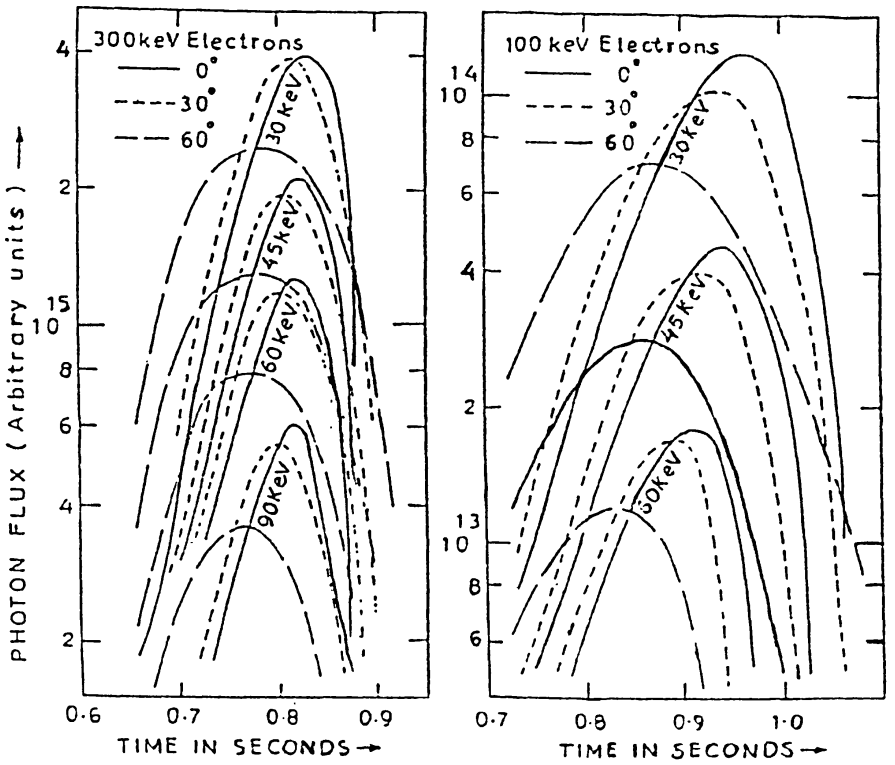

Fig. 9. Variation of total photon flux summed over all the energies as function of time for 100 and 300 keV electron energies with incidence angles 0°, 30°, and 60° (Koul *et al.* , 1988).

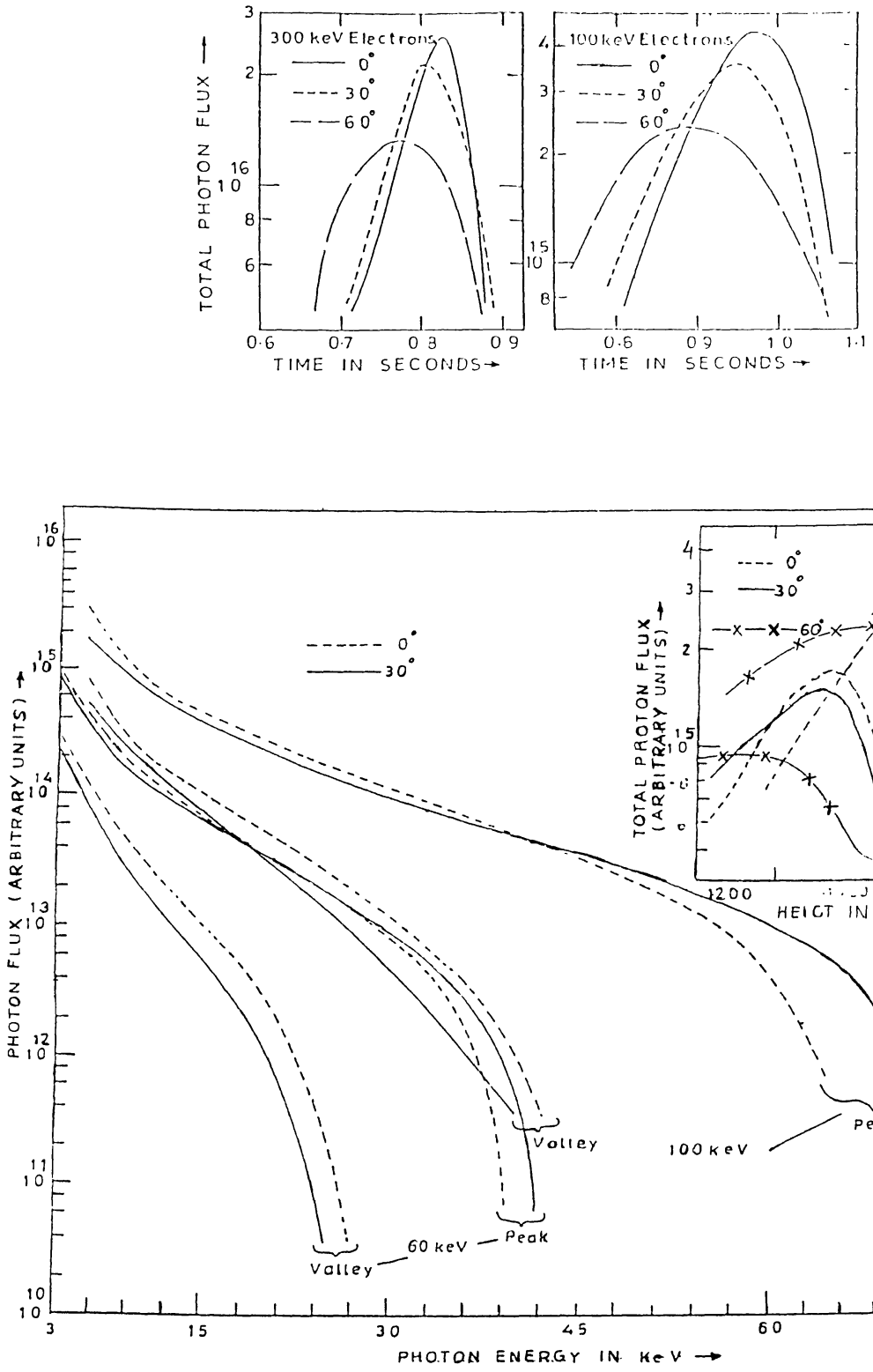

Fig. 10. Variation of photon spectrum at the peak and the valley points (heights corresponding to maximum and minimum flux) of the X-ray pulse (shown in the inset) for 0° and 30° electron incidence angles. The X-ray pulse shown in the inset is obtained by summing over all the photon energies at each height (Koul *et al.*, 1988).

injected, thus giving rise to many peaks. This explanation is also consistent with our model if we assume monoenergetic and monodirectional electron beams at start. Such electrons will give the peak X-ray flux at a height somewhere in the middle of electron path and the minimum X-ray at the absorption height of the electron. This means that the peak and the valley in the X-ray pulse are emitted from two different heights in the Sun atmosphere. By the time the streaming electrons reach the absorption point, another beam should be injected to produce the second X-ray pulse.

By summing up the X-ray flux over all the energies at different times we get only one pronounced peak (Figure 9(b)). The variation of total photon flux summed over all the energies with column density is shown in Figure 10 as an inset for 60 and 100 keV electrons, respectively, corresponding to 0° and 30° incidence angles similar to that of Figure 9(b). However, the X-ray flux due to 60° incidence for both the electron energies does not show much pronounced peak. The spectra of the X-rays at the peak (the column density somewhere in between starting and stopping column layers) and valley (at stopping column density) of the curve are also plotted in Figure 10. A look at this figure shows that the X-ray spectra at the valley is steeper compared to that at the peak. This feature can be explained by the fact that at lower column density the contribution to X-ray spectra comes from high as well as low-energy electrons whereas at higher column density the number of low-energy electrons increases due to attenuation of high-energy electrons which makes the number of low-energy photons larger resulting in the steep nature of X-ray spectra. The column density at peak and valley of the X-ray pulse are found to vary from 3.9×10^{22} cm^{-2} to 5.7×10^{20} cm^{-2} and 9.9×10^{21} cm^{-2} for 300 keV electrons.

So far we have considered the evolution of X-ray pulse accounting only the propagation effects of electrons. However, the spectra at peak and valley will depend on the nature of initial injection distribution of electrons: i.e.,

$$f(E, \theta, N) = \int_0^{\pi} \int_0^{\infty} G(E, \theta, N; E', \theta') S(E', \theta') \, dE' \, d\theta ,$$

where S is the initial injection function and G is the function obtained by the solution of transport problem using the Monte-Carlo technique. The solution of the above equation will be different from that of G with fixed E' and θ'. We have found that even with the changed solution the shape of the peak X-ray pulse retains its identity.

The observed X-ray pulses suggest an oscillatory source mechanism. However, our results show that even non-oscillatory nature of source can explain the different peaks. This is consistent with the suggestion of Kiplinger *et al.* (1983).

In flares one would expect continuous energy and pitch-angle distribution of electrons. Any injected electron beam at a discrete energy and angle becomes increasingly isotropized due to multiple scattering as it penetrates down through the solar atmosphere and assumes a continuous shape in energy and angles (Haug *et al.*, 1985). The bulk of the observed hard X-rays are emitted only after the electron beam has undergone much of the isotropization. Thus the X-ray emission will have the character of the

emission from a highly-broadened electron beam. Therefore, the curves obtained in Figures 9(a) and 9(b) can also be taken as suggestion of the effect of the continuous electron energy and angular distributions on the production of X-ray time profile.

So far we have considered the time profile of the X-ray pulse integrated over all the emission angles. However, it wil be of some interest to study the variation of X-ray spectrum and time profile at discrete observation angles. The variations of photon flux with time for 90° and 180° observation angles are plotted in Figure 11(a). The photon

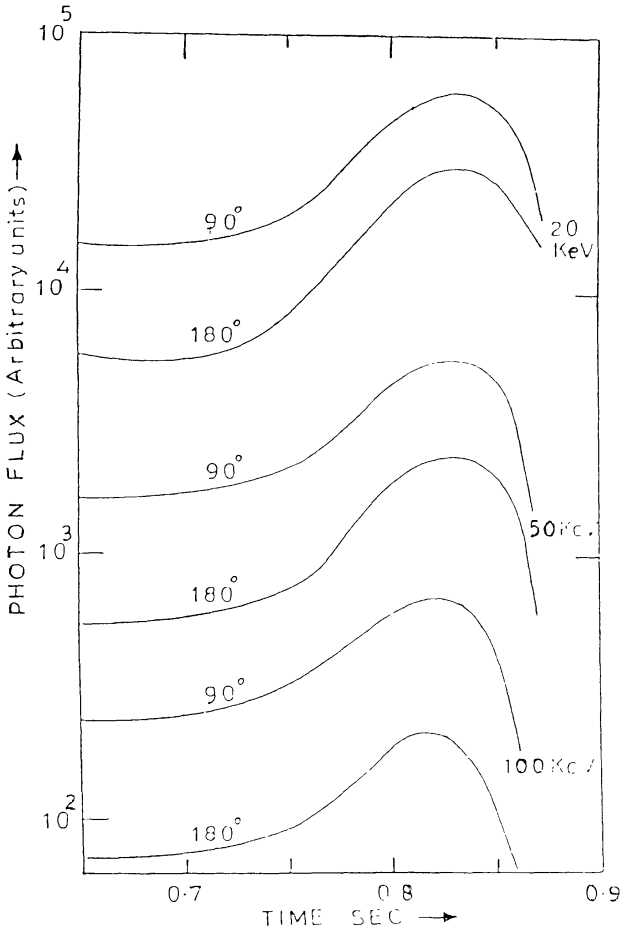

Fig. 11a. Variation of photon flux with time for observation angles 90° and 180°. The photon energies are 20, 50, and 100 keV (Koul *et al.*, 1988).

flux is always less for 180° observation angle than that for 90°. This can be easily understood in terms of the angular variation of X-rays. The nature of the curves are similar for 20 and 100 keV photons. There is appreciable difference in flux values at 90° and 180° observation angles in the beginning of the impulsive phase. However, this difference becomes less at later instance of time. For high-energy photons the difference in photon fluxes at 90° and 180° do not decrease appreciably compared to that for lower photon energies, showing that 100 keV photons are more directional. This change can be measured with two satellites separated in longitude and can also be used as a test

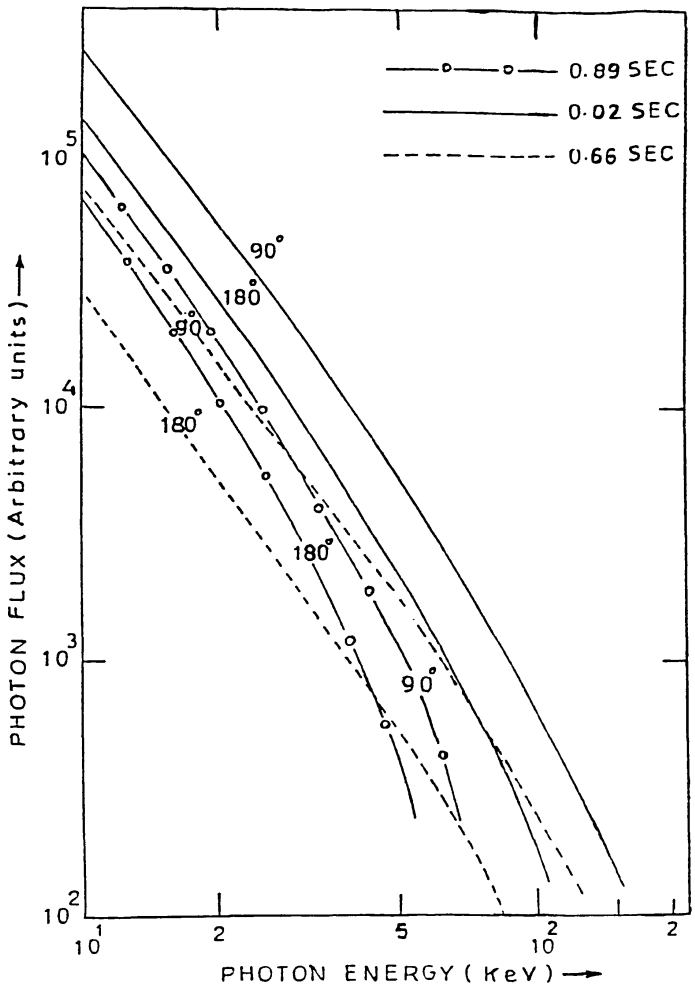

Fig. 11b. Variation of photon energy spectrum at different times for observation angles 90° and 180° (Koul *et al.*, 1988).

in support of non-thermal model. The variations of photon-energy spectrum at different times are shown in Figure 11(b). In the beginning the spectra are flatter but becomes steep afterwards. The variation of spectral index with time is similar to that reported by Kiplinger *et al.* (1984) and calculations of Lu and Petrosian (1988) as shown in their Figure 3.

6. X-Ray Polarization*

The degree of polarization is defined as

$$P = \frac{J_\perp - J_\parallel}{J_\perp + J_\parallel} , \tag{8}$$

where $J_\perp$ and $J_\parallel$ are the fluxes of X-radiation polarized perpendicular and parallel, respectively, to the plane of emission. The intensities $J_\perp$ and $J_\parallel$ emitted as

* The major portion on polarization studies has been derived from Haug *et al.* (1985b).

bremsstrahlung from the volume V by monodirectional electrons and measured at Earth distance R are given by

$$J_{\perp}(E, \vartheta) = \frac{n_{\mathrm{H}} V}{R^2} \int_{\varepsilon}^{\infty} \frac{\mathrm{d}j_e \, \mathrm{d}^2\sigma_{\perp}}{\mathrm{d}E \, \mathrm{d}\varepsilon \, \mathrm{d}\Omega} \, \mathrm{d}E \quad \text{photons cm}^{-2}\,\text{s}^{-1}\,\text{keV}^{-1}\,, \tag{9}$$

and

$$J_{\parallel}(E, \vartheta) = \frac{n_{\mathrm{H}} V}{R^2} \int_{\varepsilon}^{\infty} \frac{\mathrm{d}j_e \, \mathrm{d}^2\sigma_{\parallel}}{\mathrm{d}E \, \mathrm{d}\varepsilon \, \mathrm{d}\Omega} \, \mathrm{d}E \quad \text{photons cm}^{-2}\,\text{s}^{-1}\,\text{keV}^{-1}\,, \tag{10}$$

where ε is the photon energy; ϑ, angle between the momenta of incoming electrons and photons; n_{H}, hydrogen number density; E, kinetic energy of electrons; $\mathrm{d}j_e/\mathrm{d}E$, differential electron flux (electrons $\mathrm{cm}^{-2}\,\mathrm{s}^{-1}\,\mathrm{keV}^{-1}$); $\mathrm{d}^2\sigma_{\perp}/\mathrm{d}\varepsilon\,\mathrm{d}\Omega$, $\mathrm{d}^2\sigma_{\parallel}/\mathrm{d}\varepsilon\,\mathrm{d}\Omega$, differential cross-section of bremsstrahlung polarized perpendicular and parallel, respectively, to the plane of emission.

The bremsstrahlung polarized cross-sections have been derived in the Born approximation by Gluckstern and Hull (1953). We have used these formulae corrected by a Coulomb factor (Elwert, 1939) together with the electron distributions computed in Section 2. In the problem to be considered now, Equations (9) and (10) cannot be applied directly since the electrons penetrating the solar atmosphere are not monodirectional and so no unique plane of emission exists. In our model (Haug *et al.*, 1985) the primary flare electrons have been accelerated to the energy E_0. As they traverse the ambient plasma, the originally monodirectional electron beam broadens by collisions. The resulting angular distribution is, in absence of a magnetic field, axial symmetric around the primary beam direction given by the original electron momentum P_0. The X-ray polarization has, therefore, to be referred to the plane of observation spanned by P_0 and the line-of-sight k; it is given by Haug (1972) as

$$P = \cos(2\psi)\,\frac{J_{\perp} - J_{\parallel}}{J_{\perp} + J_{\parallel}}\,, \tag{11}$$

where the angle ψ is defined by

$$\cos\psi = \frac{(\mathbf{p} \times \mathbf{k}) \cdot (\mathbf{p}_0 \times \mathbf{k})}{|\mathbf{p} \times \mathbf{k}|\,|\mathbf{p}_0 \times \mathbf{k}|}\,; \tag{12}$$

in which $\mathbf{p}$ denotes the instantaneous electron momentum. Equation (11) was originally derived for electrons spiralling around a magnetic field with constant pitch-angle α. So the same formula can also be used if a uniform magnetic field perpendicular to the stratification of the atmosphere is present, for electrons incident in the field direction

(incidence angle $\alpha_0 = 0$) as well as in the absence of magnetic field for $\alpha_0 = 0$. To apply it to initial angles α_0 different from zero one has to consider a conical angular distribution of the initial electrons around the direction normal to the stratification. The angle to be inserted into Equation (9) to (11) can be expressed in terms of the angle α between p and the original electron momentum p_0, the angle θ between p_0 and the line-of-sight k, and the azimuth angle ϕ of the vector **p** relative to p_0,

$$\cos\vartheta = \cos\alpha\cos\theta + \sin\alpha\sin\theta\cos\phi\,. \tag{13}$$

The intensities of X-rays polarized, respectively, perpendicular and parallel to the plane of reference and emitted from the kth layer are obtained by integration over the instantaneous energies and angles of the electrons traversing the layer. The difference and the sum of these intensities denoted by I_D and I_S, respectively, are given (omitting constant factors) by

$$I_D(\varepsilon, \theta, \bar{N}_k; E_0) = \Delta N_k \int_{\varepsilon}^{\infty} dE \int_0^{\pi} \frac{d\alpha}{|\cos\alpha|} \int_0^{2\pi} \frac{d\phi}{2\pi} \cos(2\psi)\,, \tag{14}$$
$$f(E, \alpha, \bar{N}_k; E_0)\left(\frac{d^2\sigma_\perp}{d\varepsilon\, d\Omega} - \frac{d^2\sigma_\parallel}{d\varepsilon\, d\Omega}\right)$$

and

$$I_S(\varepsilon, \theta, \bar{N}_k; E_0) = \Delta N_k \int_{\varepsilon}^{\infty} dE \int_0^{2\pi} \frac{d\alpha}{|\cos\alpha|} \int_0^{2\pi} \frac{d\phi}{2\pi} \cos(2\psi)\,, \tag{15}$$
$$f(E, \alpha, \bar{N}_k; E_0)\left(\frac{d^2\sigma_\perp}{d\varepsilon\, d\Omega} + \frac{d^2\sigma_\parallel}{d\varepsilon\, d\Omega}\right).$$

The polarization at a given column density N_k can be written as

$$P(\varepsilon, \theta, \bar{N}_k; E_0) = I_D(\varepsilon, \theta, \bar{N}_k; E_0)/I_S(\varepsilon, \theta, \bar{N}_k; E_0)\,. \tag{16}$$

The total polarization is obtained by summing up I_D and I_S over all contributing layers, i.e., up to the column density $N_{\text{stop}}(E_0)$, where all the electrons of initial energy E_0 have been completely stopped,

$$P_{\text{tot}}(\varepsilon, \theta, E_0) = I_{D,\,\text{tot}}(\varepsilon, \theta; E_0)/I_{s,\,\text{tot}}(\varepsilon, \theta; E_0) =$$
$$= \sum_K I_D(\varepsilon, \theta, N_k; E_0) \Big/ \sum_K I_S(\varepsilon, \theta, \bar{N}_k; E_0)\,. \tag{17}$$

Equations (14) and (15) give the quantities which one needs for the calculation of bremsstrahlung polarization. $I_S(\varepsilon, \theta, \bar{N}_k; E_0)$ is proportional to the X-ray flux emitted from the kth layer with the average column density N_k by electrons with initial energy E_0. Figure 12 depicts the variation of the X-ray flux as a function E_0 and

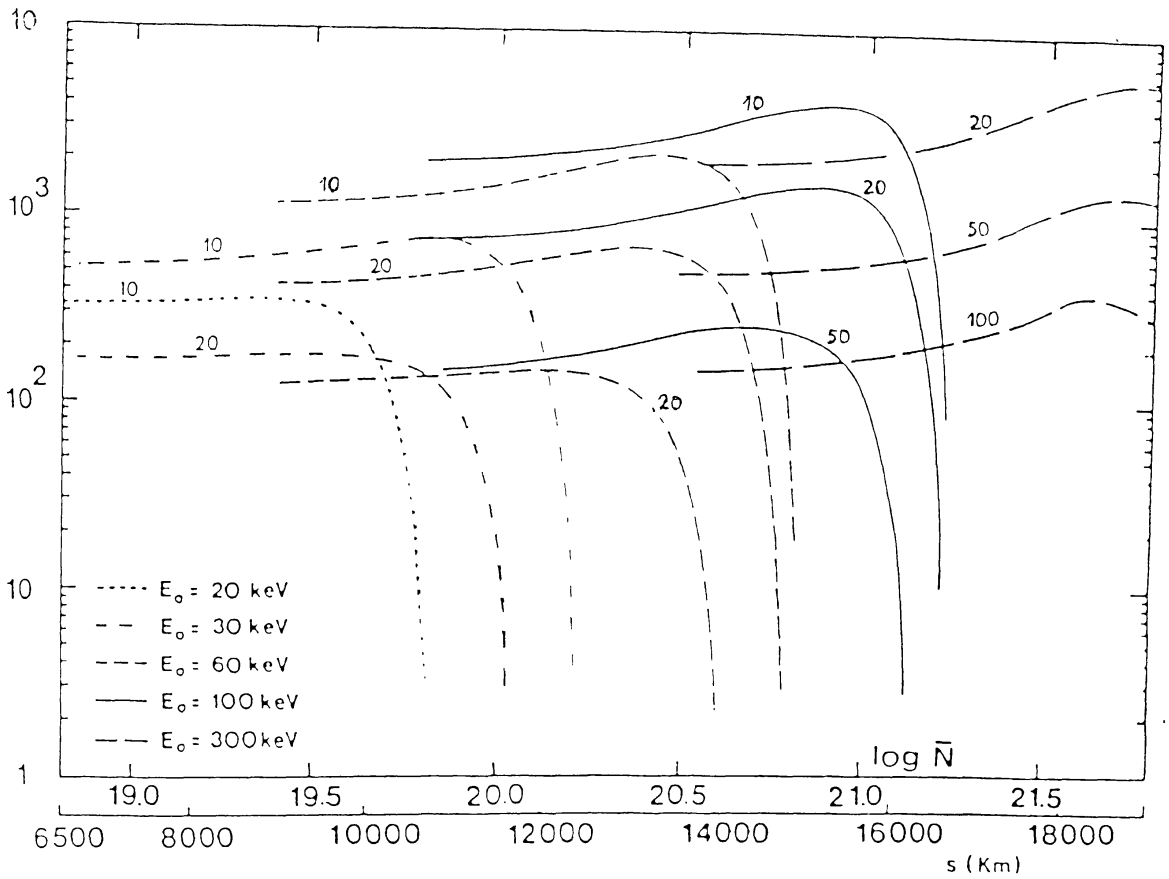

Fig. 12. Photon flux $I_s(\varepsilon, \theta, \bar{N}; E_0)$ for the observation angle $\theta = 90°$ as a function of the mean column density $\bar{N}$ for various photon energies ε and initial electron energies E_0. The curves are labelled by the photon energy ε in keV. The intensities (in arbitrary units) refer to the layers of column densities N. The lower abscissa scale gives the altitudes corresponding to an exponential law for the density (see text) (Haug *et al.*, 1985b).

photon energies ε. For better illustration a second scale on the abscissa gives the altitudes S (counted downward from the site of electron injection) corresponding to the column densities $N(S)$ according to the exponential law for the proton number.density $n = n_0 e^{as}$. As parameters typical of flare conditions we chose $n_0 - 10^9$ cm^{-3} and $a = 5.5 \times 10^{-3}$ km^{-1}. The figure shows that the number of photons emitted in a layer increases slowly and then decreases steeply with increase in column density. The column density for which this decrease occurs depends on the electron energy E_0 and less distinctly on the photon energy ε. For fixed photon energy ε and increasing electron energy E_0 the decrease is shifted to higher column densities. This behaviour is easily explained in terms of the electron stopping power as a function of E_0. At fixed electron energies E_0 the decrease is shifted to lower column densities with increasing photon energy. This can be understood by the fact that less and less electrons with energies sufficient for emission of energetic photons are present at higher column densities.

Polarization measurements have been performed only for relatively soft photons of $\varepsilon = 10$ to 20 keV. Therefore, we will restrict ourselves to these energies in the following.

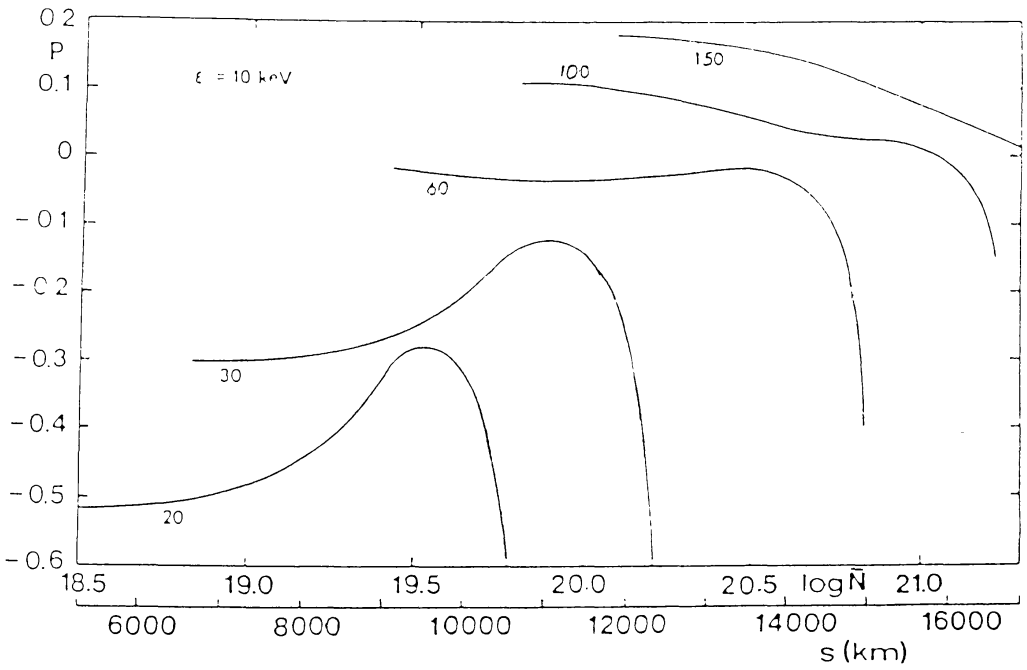

Fig. 13. Degree of polarization P for $\varepsilon = 10$ keV and $\theta = 90°$ as a function of the mean column density $\overline{N}$ and altitude s. The labels refer to the initial electron energy E_0 in keV (Haug *et al.*, 1985b).

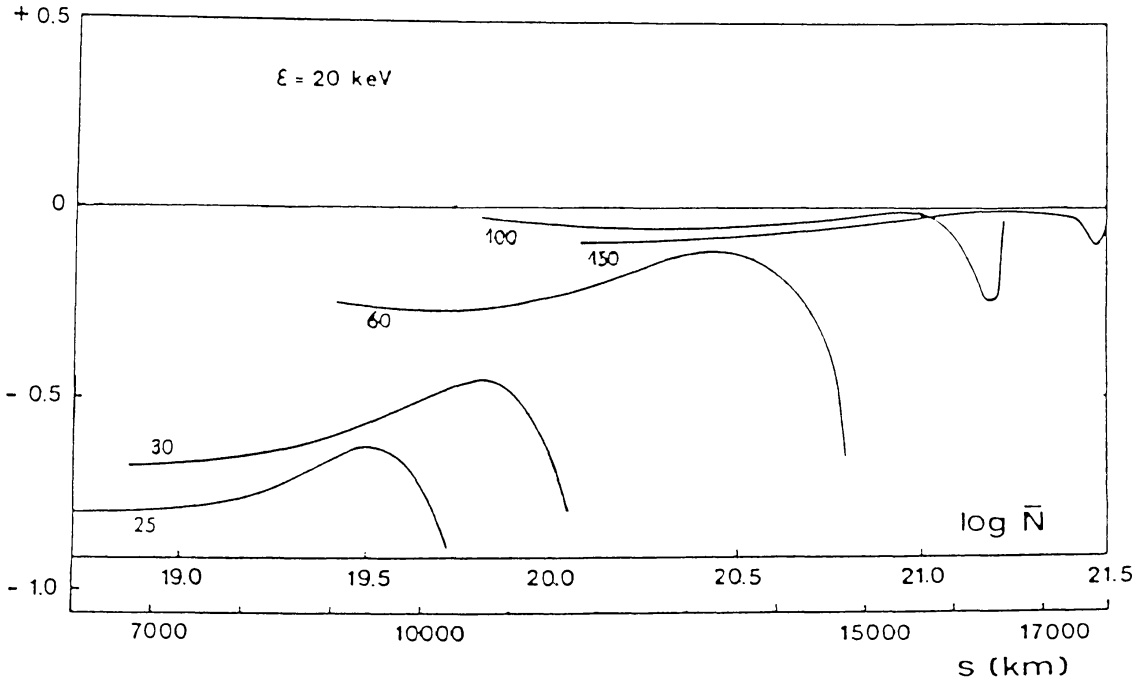

Fig. 14. Degree of polarization P for $\varepsilon = 20$ keV and $\theta = 90°$ as a function of the mean column density $\overline{N}$ and altitude s. The labels refer to the initial electron energy E_0 in keV (Haug *et al.*, 1985b).

Figures 13 and 14 show the degree of polarization P as a function of the mean column density N for $\theta = 90°$ and various energies E_0 of the primary electrons. The photon energy is 10 keV in Figure 13. P is mostly negative, i.e., the X-rays are polarized parallel to the plane of observation. For $E_0 \leq 60$ keV the absolute value of the polarization decreases with increasing column density. After reaching a maximum, P increases steeply near the stopping power N_{stop} (Haug *et al.*, 1985). At column densities slightly smaller than N_{stop} the mean energy of the electron is not much greater than the energy of the emitted X-ray quanta. These are, therefore, emitted near the short-wavelength limit. It is well known in the theory of bremsstrahlung that the polarization is negative and its absolute value is maximum under these conditions (Sommerfeld, 1931; Gluckstern and Hull, 1953; Korchak, 1967). For decreasing values of the ratio between photon energy and electron energy the degree of polarization becomes zero and then attains positive values. Therefore, P changes sign for high initial electron energies E_0 and sufficiently low column densities $\overline{N}$.

The X-ray polarization for photon energy $\varepsilon = 20$ keV is plotted in Figure 14. Here P is negative for values of the initial energy E_0 up to 150 keV.

Figure 15 shows the degree of polarization as a function of the observation angle θ

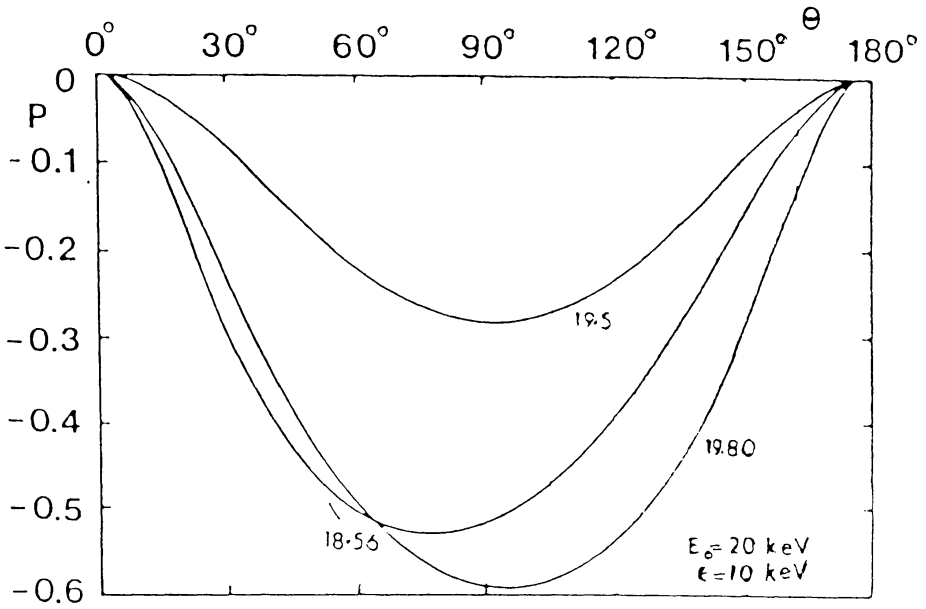

Fig. 15. Degree of polarization P as a function of observation angle ϑ for $E_0 = 20$ keV, $\varepsilon = 10$ keV, and various column densities N. The curves are labelled by $\log N$ (Haug *et al.*, 1985b).

for 10 keV photons emitted from electrons of initial energy $E_0 = 20$ keV and various column densities. The curve for $\log \overline{N} = 18.56$ can be taken as reference for nearly monoenergetic and monodirectional electrons (cf. Figure 12). Then the two other curves give an idea about the changes in the polarization due to scattering. As discussed in connection with Figure 13, the absolute value of the polarization is higher at the beginning of the electron path, becomes smaller at increasing column densities, and

increases again near the stopping column density N_{stop}. The peak of the polarization curves is always near $\theta = 90°$ even though it shifts to higher angles of observation with increasing $\overline{N}$.

For flares occurring near the solar limb it is, in principle, possible to observe the polarization as a function of height above the limb. However, as can be seen from the abscissae of Figures 12–14 this would require an angular resolution of less than 10″ (corresponding to 7000 km on the solar surface); hence, such measurements have not been carried out so far. Therefore, the intensities I_D and I_S are summed over all layers. The resulting polarization $P_{tot}(\varepsilon, \theta; E_0)$ is given by Equation (17) and is plotted in Figure 16 as a function of the initial electron energy E_0 for photon energies $\varepsilon = 10$ and

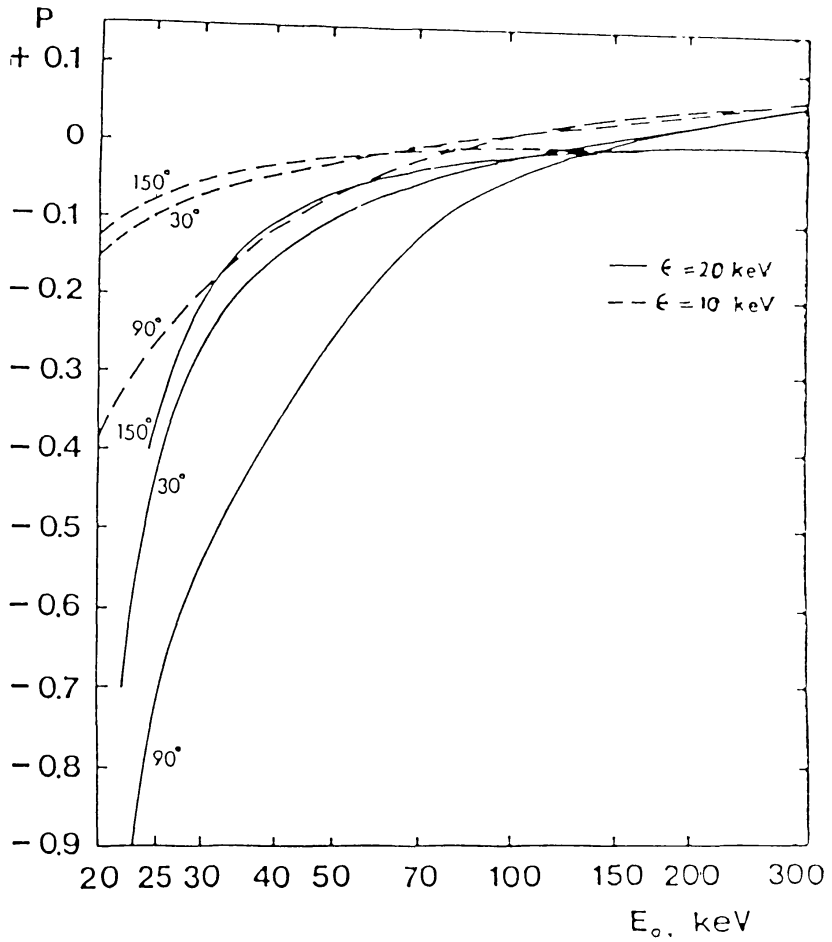

Fig.16. Total degree of polarization P as a function of the initial energy E_0 for $\varepsilon = 10$ and 20 keV and various observation angles (Haug *et al.*, 1985b).

20 keV and various observation angles. As in Figures 13 and 14, the absolute value of the degree of polarization is highest near the the short wavelength limit, i.e., for low electron energies E_0. In accordance with Figure 15, the maximum polarization occurs for angles $\theta \simeq 90°$.

So far we have considered polarization characteristics of X-rays from initially mono-

energetic electron beams. However, observations of hard X-radiation during flares (Kane and Anderson, 1970) are consistent with electron energy distribution in form of a power-law

$$f(E) \simeq E^{-\delta}, \tag{18}$$

where δ is the spectral index. Therefore, we have calculated the polarization of X-rays emitted from electrons with injection spectra of the form (18). In this case the intensities I_D and I_S are given by

$$I_D(\varepsilon, \theta, \bar{N}; \delta) = \int_{\varepsilon}^{\infty} I_D(\varepsilon, \theta, N; E_0) E_0^{-\delta} \, dE_0 \tag{19}$$

and

$$I_S(\varepsilon, \theta, \bar{N}; \delta) = \int_{\varepsilon}^{\infty} I_S(\varepsilon, \theta, N; E_0) E_0^{-\delta} \, dE_0 \, . \tag{20}$$

The polarization is then defined as

$$P(\varepsilon, \theta, \bar{N}; \delta) = I_D(\varepsilon, \theta, \bar{N}, \delta)/I_S(\varepsilon, \theta, \bar{N}, \delta) \, . \tag{21}$$

It is expendient to normalize the intensity I_S by the average value

$$\bar{I}_S(\varepsilon, \bar{N}, \delta) = \frac{1}{2} \int_0^{\pi} I_S(\varepsilon, \theta, \bar{N}, \delta) \sin\theta \, d\theta \, . \tag{22}$$

Figures 17 and 18 show the directivity $I_S/\bar{I}_S$ and polarization P of the X-radiation for the photon energy 20 keV, column density $N = 10^{19}$ cm^{-2}, and the spectral indices $\delta = 4$ and 6. The column density selected is representative of a layer where the energy and angular dispersion of the injected electron beam is appreciable but the electrons are not yet stopped (Figure 12). If we assume a constant coronal particle density of $(3\text{–}5) \times 10^9$ cm^{-3} as considered by LP, $N = 10^{19}$ cm^{-2} corresponding to the path-length $S = 20\,000$ to $30\,000$ km, i.e., the electrons should have reached the transition zone.

Both sets of curves are not much dependent on the value of δ. The directivity ratio is $I_{S,\max}/I_{S,\min} \simeq 9$ to 10 with the X-rays beamed around $\theta = 60°$. The polarization reaches a maximum of 65% to 70% near $\theta \simeq 90°$.

The curves of Figures 17 and 18 can be compared with the results of LP. Their models differ from ours with respect to:

(1) The electrons injected with a power-law spectrum (spectral index δ) are in general not monodirectional but have a Gaussian distribution in pitch angles $\sim \exp(-\alpha^2/\alpha_0^2)$.

(2) LP consider a magnetic field structure in the form of a semi-circular loop. The loop is divided into several segments with a mean magnetic field direction **B**. The rate

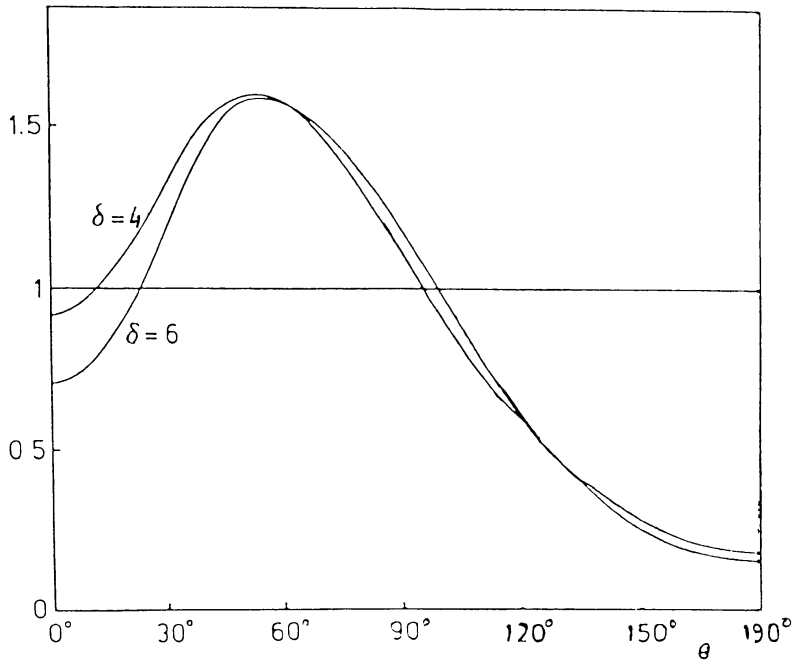

Fig. 17. Directivity of the X-radiation from electrons injected with a power-law spectrum (spectral index δ). The photon energy is 20 keV and the average column density $\overline{N} = 10^{19}$ cm^{-2} (Haug *et al.*, 1985b).

of convergence of the magnetic field is characterized by the parameter $\mathrm{d} \ln B/\mathrm{d}Z$ where Z is a dimensionless column density along the loop.

Our results correspond to LP's calculations of the directivity and polarization for the segments. The various models of LP are classified according to the parameters α_0^2 and $\mathrm{d} \ln B/\mathrm{d}Z$. Their model 5 with $\delta = 5$, $\alpha_0^2 = 0.04$, and $\mathrm{d} \ln B/\mathrm{d}Z = 0$, i.e., uniform magnetic field, is most similar to ours. LP give the characteristics of X-rays integrated over the whole loop as well as the variation with column depth.

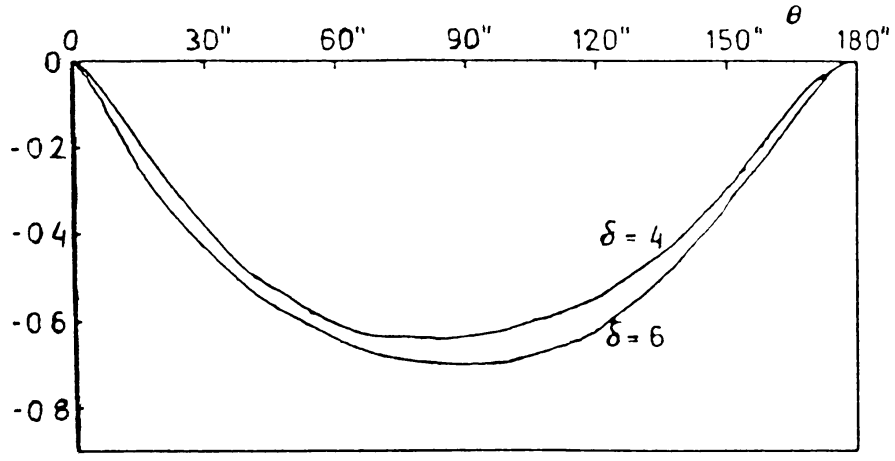

Fig. 18. X-ray polarization from electrons injected with a power-law spectrum (spectral index δ). The photon energy is 20 keV and the average column density $\overline{N} = 10^{19}$ cm^{-2}.

The directivity curves (Figure 17) resemble much LP curves for loop segments 1 and 5 (their Figure 10), corresponding to column density $3.4 \times 10^{17}\,\mathrm{cm}^{-2}$ and $3.2 \times 10^{18}\,\mathrm{cm}^{-2}$ and the photon energy 16 keV (note that LP's local angle θ is the direction away from the photosphere). Our directivity ratio at $N = 10^{19}\,\mathrm{cm}^{-2}$ is a little higher than LP's ratio for segment 5. This small discrepancy may be due to our higher photon energy.

The polarization curves of Figure 18 are nearly identical to LP's curve for $E = 16$ keV and loop segment 5 (their Figure 11). Of course, the model of LP with isotropic injection and/or with a strongly corresponding magnetic field yield smaller directivity ratios and lower degree of polarization.

The X-rays integrated over all layers are characterized by the intensities

$$I_{D,\,\mathrm{tot}}(\varepsilon, \theta; \delta) = \int_{\varepsilon}^{\infty} I_{D,\,\mathrm{tot}}(\varepsilon, \theta; E_0) E_0^{-\delta}\,\mathrm{d}E_0 \tag{23}$$

and

$$I_{s,\,\mathrm{tot}}(\varepsilon, \theta; \delta) = \int_{\varepsilon}^{\infty} I_{s,\,\mathrm{tot}}(\varepsilon, \theta; E_0) E_0^{-\delta}\,\mathrm{d}E_0\,, \tag{24}$$

respectively. Figure 19 depicts the X-ray intensities $I_{s,\,\mathrm{tot}}(\varepsilon, \theta, E_0)$ and $I_{D,\,\mathrm{tot}}(\varepsilon, \theta, E_0)$ (see Equation (17)) as a function of E_0 for the photon energy 20 keV and observation angles $\theta = 30°$ and $90°$.

The total intensity I_S is higher for $\theta = 30°$ than for $90°$. This can be explained by the relativistic beaming of the bremsstrahlung production (Elwert and Haug, 1971; Petrosian, 1973). The total intensity increases with the initial electron energy E_0. The figure shows that the energy and the angular dependence of $I_{s,\,\mathrm{tot}}$ and $I_{D,\,\mathrm{tot}}$ is different. The integrands of Equations (23) and (24) for spectral indices $\delta = 2$ and 6 are also plotted in Figure 19 (in arbitrary units). The curves demonstrate that for steep electron spectra (high δ) only the initial energies E_0 close to the photon energy give significant contribution, whereas for hard electron spectra (small δ) one has also to take into account high values of E_0.

The total polarization from electrons with a power-law distribution of initial energies is shown in Figure 20 as a function of the spectral index δ for $\theta = 30°$, $90°$, and $150°$, and $\varepsilon = 10$ and 20 keV. For the photon energies considered the degree of polarization is virtually independent of ε whereas it varies with θ. This is in agreement with LP's model 5. The absolute value of P is highest for steep electron spectra (large δ). This can be explained by the large contribution of electrons with low initial energy E_0 corresponding to the short-wavelength limit of bremsstrahlung production, i.e., the ratio ε/E is near unity. Therefore, it is be expected that X-ray flares with steep spectra are more strongly polarized than flares with harder spectra. This argument must, however, be applied with caution since the effect of the spectral index will be significant only if the polarization is measured at sufficiently high photon energies where the contribution of the unpolarized background is low.

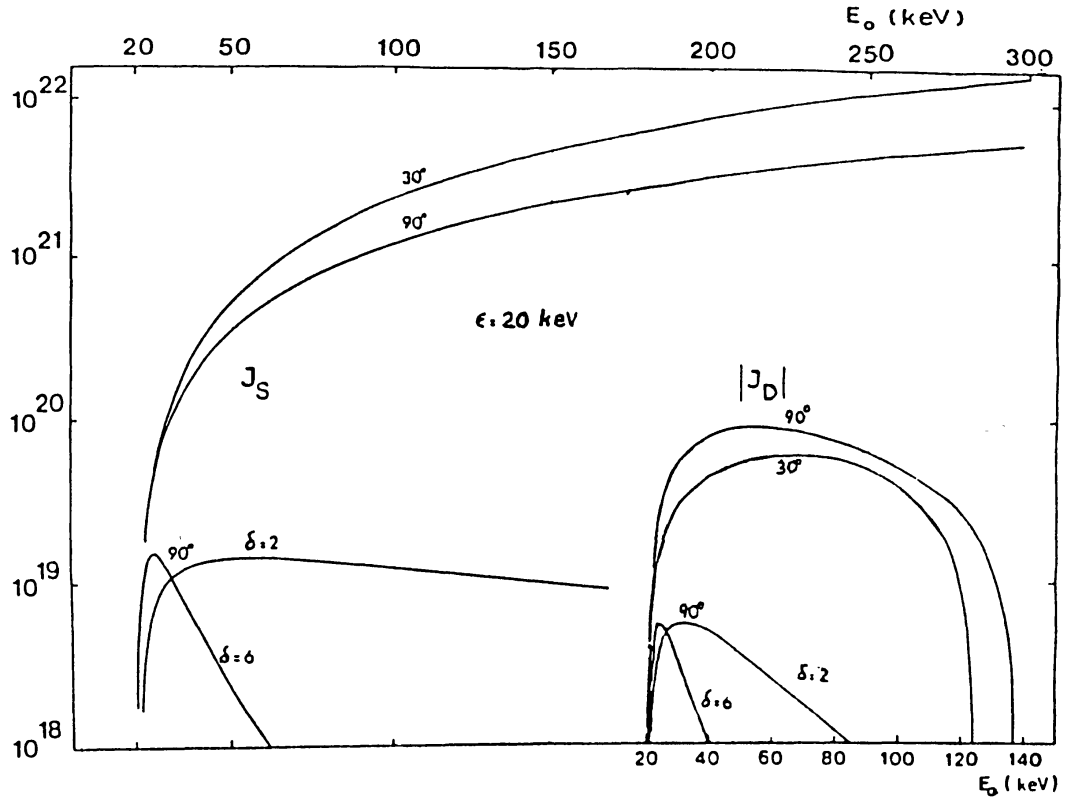

Fig. 19. Total photon fluxes $I_{s,\,\mathrm{tot}}(\varepsilon, \theta; E_0)$ and $|I_{D,\,\mathrm{tot}}(\varepsilon, \theta; E_0)|$ as a function of initial energy E_0 for $\varepsilon = 20$ keV and observation angles $\theta = 30°$ and $90°$. The lower curves show the respective intensities weighted by the power-law $E_0^{-\delta}$ for $\delta = 2$ and $\delta = 6$ (in arbitrary units) (Haug *et al.*, 1985b).

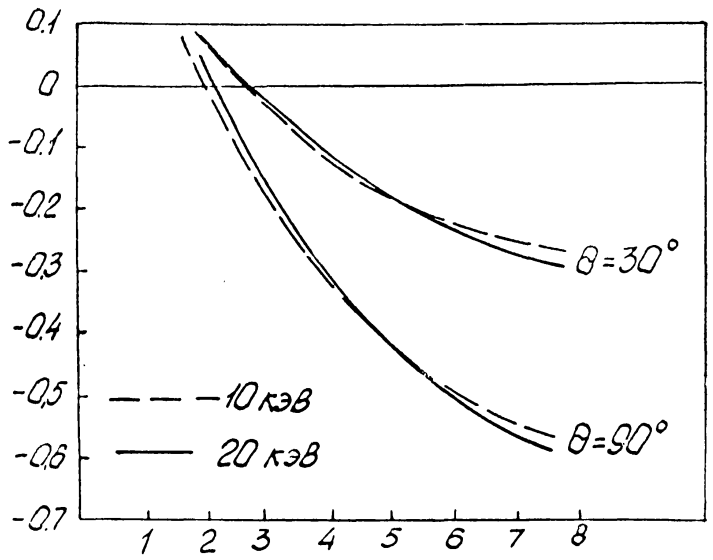

Fig. 20. Total polarization for electrons injected with a power-law spectrum as a function of the spectral index for photon energies $\varepsilon = 10$ and 20 keV and various observation angles (Haug *et al.*, 1985b).

For $\delta = 5$ the degree of polarization is much higher than in model 5 of LP (their Figure 16). The main reason for the strong reduction in P is the loop geometry used by LP. As a consequence their global angle θ is different from our observation angle θ. In the LP models the electrons are injected at the top of the magnetic loop with mean direction parallel to the solar surface, and following the loop curvature, the electrons arrive to the chromosphere perpendicular to the surface. For a limb flra ($\theta = 90°$), e.g., the polarization of the X-radiation emitted by the electrons at the top of the loop is $P \sim 0$. Bearing in mind that the degree of polarization is approximately proportional $\sin^2 \vartheta$ (Elwert and Haug, 1970) and that the angular dispersion of the electrons becomes maximum near the footpoints of the loop ($\vartheta = 90°$), it is obvious that the polarization is strongly reduced in the models of LP.

For comparison of our results with observations, one has to bear in mind that the assumption of an initially monodirectional electron beam is highly idealized. The theoretical degrees of polarization may, therefore, be considered as upper limits. Besides, in order to meet the suppositions of the theory, the observations have to be performed during the impulsive phase of the X-ray flare where the accelerated electrons are not yet thermalized by collisions. The measurements of X-ray polarization is extremely difficult, even without spatial resolution. Therefore, only a few observational results are available. The first observations of X-ray polarization during solar flares by Tindo *et al.* (1970) resulted in high polarization degrees up to 0.4, however, with an uncertainty of about 50%. In the second series of measurements (Tindo *et al.*, 1972a, b) the maximum degrees of polarization were between 10% and 20%. The most recent observations by Tindo *et al.* (1976) with an improved polarimeter were performed near the minimum of the solar cycle (May to November, 1974). Thus, only 3 flares with sufficiently intense hard X-rays could be observed and the resulting degree of polarization were quite low ($\leq 5\%$). We feel that these weak events are not representative of typical hard X-ray flares; besides, no spectral data are available for these flares. Therefore, we ocmpare our theoretical results with the measurements of 1970 (Tindo *et al.*, 1972a, b) even though the more recent experiments appear to be more accurate. The energy of photons detected by the X-ray polarimeter was $\varepsilon \simeq 15$ keV. During the impulsive phase of the flares of 24 October (importance 2*N*) and 5 November, 1970 (importance 3*B*) the X-ray spectra could be fitted by power laws with spectral index $\gamma \simeq 4$. This corresponds to the electron spectral index $\delta = 5$ (Brown, 1971). The locations of the optical flares on the solar disk were N 14 E 75 and S 12 E 35, respectively. If we assume electron injection downwards in radial direction which agree with the orientation of the polarization vector (Tindo *et al.*, 1972b), the respective angles of observation were $\theta_1 = 105°$ and $\theta_2 = 144°$. Then theoretical degrees of polarization according to Figure 20 are $|P_1| \simeq 0.35$ and $|P_2| \simeq 0.17$ as against the maximum observed values $P_1 \simeq 0.16$ and $P_2 \simeq 0.21$.

Whereas the measured X-ray polarization is of the same order of magnitude as predicted by the theoretical model, the polarization in the flare on 24 October was lower than that of the flare on 5 November, contrary to theoretical expectations. We consider three explanations:

(1) The injection of energetic electrons is not vertically downward, so that the observation angle cannot be inferred from the location of the optical flare.

(2) The hard X-ray flux and, hence, the number of nonthermal electrons injected during the flare of 24 October was lower than that of the flare on 5 November. In our calculations a possible contribution of thermal X-ray background due to thermal electrons would reduce the degree of polarization.

(3) The injected electrons will not be strictly monodirectional. Their angular spread might be larger in the weaker flare.

The first explanation seems to be ruled out by the analysis of Tindo *et al.* (1972b).

Recently, Tramiel *et al.* (1984) have flown an X-ray polarimeter on the third flight of the space shuttle Columbia during a 28-hour period of solar observations, seven X-ray flares were strong enough to allow meaningful polarization measurements. Due to a preflight contamination problem the instrument had to be calibrated in-flight against two flares near the centre of the solar disk which are assumed to be unpolarized. In any of the other flares no statisticaly significant polarization was detected in the 5 to 20 keV and, upper limits (99% confidence level) ranging from 2.5% to 12.7%. These results disagree with the present predictions and with most LP models. In our opinion, these observations do not, however, invalidate the nonthermal models of solar flares with beamed electrons for the following reasons:

(1) As pointed out above, the polarization measurements have to be performed during the impulsive phase(s) of an X-ray flare while the data analysis of Tramiel *et al.* is based on count rates integrated over the entire flare duration. The impulsive phase was analyzed separately only for one flare but even there the integration time was as long as 1.6 min. Nevertheless, it resulted in higher degrees of polarization compared with the analysis of the same flare for the whole observing period, even though the polarization is still lower than predicted by the 'conventionally' beamed models.

(2) All the seven X-ray flares analysed were relatively weak, the strongest one being classified as M2.1. For instance, one of the flares which was also observed by ISEE-3 had a peak X-ray flux at 10 keV more than 20 times weaker than the peak fluxes of the 1970 flares discussed above. This results on the one hand in poor counting statistics, on the other hand it is expected that the polarization of large X-ray flares is higher.

(3) The X-ray spectra of weak flares are generally quite steep. Therefore, the dominant contribution to the 5 to 20 keV band comes from soft X-rays with the significant admixture of a thermal background. Some indication of this effect is provided in Table II of Tramiel *et al.*, where the polarization is largest in the highest energy channels.

(4) Even though Tramiel *et al.* proceeded very carefully in the reduction of the data, the analysis was handicapped by the contamination of the scattering targets. Thus they had to make assumptions which though reasonable, give additional uncertainties to the results.

For amore throrough interpretation of the theoretical results it is highly desirable to have more observational data. The greatest progress is to be expected from investigation with good spatial resolution providing information about the dependence of X-ray polarization on the source location on the Sun. Due to their extreme complexity the only

possibility to perform in near-future experiments with a modest resolution will be the use of the method of stereoscopic observations of limb flares as carried out by Kane *et al.* (1982).

7. Summary and Conclusions

On comparing our results with the recent observations we conclude that:

(i) The spectral index varies along the loop (Figure 3), the spectrum is hardest at the injection site and becomes progressively softer with the increase in depth of penetration (higher column densities) for monoenergetic incident electrons. However, in the case of power-law distributions the spectrum becomes harder. This aspect can be used to test various theories of electron acceleration. Such spatial dependence of the spectral index has not been measured but the recent observations of fine time structures in X-ray time profiles do reveal a harder spectra at the peak compared to that at the valley of the X-ray pulse (Kane *et al.*, 1983). By correlating the temporal and spatial peaks following the line of reasoning given by Emslie (1983) a look at Figure 10 shows that the peak and the valley of the observed X-ray pulse would be emitted from two different heights in the solar atmosphere.

(ii) The integrated X-ray flux measured by ISEE-3 and PVO spacecrafts (Kane *et al.*, 1980; Figure 1) correspond well with our spatially integrate X-ray flux (Figure 4). In our calculations we have presented the picture of only one incident electron energy. It has, however, been found that the nature of the curve remain the same over a large energy range of incident electron energies from 60 to 500 keV. However, the column density at which the anisotropy ratio changes increases with increase in energy of the incident electrons. The variation in photon spectra with electron incidence angle is found to be insignificant (Figure 3(b)).

We also find that the integrated X-ray emission from the whole source has the character of the emission from a highly broadened electron beam, independent of the original degree of electron beaming at the injection.

(iii) The calculations of directivity of the hard X-rays (Figures 6(a), 6(b), and 7) and their comparison with the observed directivities of the hard X-rays (Kane *et al.*, 1980) reveals that the X-ray source is almost isotropic for lower difference angles. However, out calculations do point out that for difference angles larger than 60° one should observe anisotropy at least at the start of the impulsive phase. The inclusion of photospheric back-scattering of the photon directed downwards may further reduce the anisotropy, in addition to the reduction already produced by the dispersion in electron distributions due to Coulomb collisions. As shown by Bai and Ramaty (1978) the angular distribution of high-energy photons are not modified significantly by Compton scattering, which indicates that there should be some observable anisotropy even after allowance for Coulomb collisions and Compton back-scattering.

(iv) The calculation of the anisotropy quotient as a function of column density (Figure 6(a)) gives some important clues regarding the electron acceleration. The X-ray flux ratio observed by the ISEE-3 and PVO spacecraft as a function of time (Figure 2

of Kane *et al.*, 1982) for 150 keV photons shows that the ratio decreases at the start of the impulsive phase and then increases towards the end of the impulsive phase. The ratio attains a fairly large constant value during the gradual phase for approximately 5 min. On comparing our calculated ratio of 100 and 150 keV photons as a function of column density (Figure 5) with these observations we find that the nature of the curves are similar. In the thick-target geometry the high-energy electrons accelerated at neutral points high in the corona and injected towards the photosphere will reach the absorption point within a fraction of a second. However, the observatons of Kane *et al.* (1980) show that the trend persists for more than 5 min. Although it is not a general feature but if observed such long period gradual phase emissions cannot be explained unless we assume either the confinement of the particles in the magnetic field geometry injected at higher angles or a continuous injection of the electron beam. The second possibility of continuous injection of the electron beam seems to be more plausible.

(v) The polarization calculations and its comparison with observation favour beamed thick-target model.

The results reported in this paper support X-ray generation at low altitudes in the thick-target bremsstrahlung model (Koul *et al.*, 1985). The energetic source electrons are most likely accelerated continuously at a neutral sheet formed in the corona from where they propagate downward toward the photosphere. The modulation of the particles injection/acceleration and the propagation of the particles gives rise to the observed characteristics of the X-ray emissions.

References

Acton, L. W., Canfield, R. C., Gunkler, T. A., Hudson, H. S., Kiplinger, A. L., and Leibacher, J. W.: 1982, *Astrophys. J.* **263**, 409.

Bai, T.: 1982, in R. E. Lingenfelter, H. S. Hudson, and D. M. Worrall (eds.), *X-ray Transients and Related Astrophysics,* American Institute of Physics, New York, p. 409.

Bai, T. and Ramaty, R.: 1978, *Astrophys. J.* **219**, 705.

Brown, J. C.: 1971, *Solar Phys.* **25**, 158.

Brown, J. C.: 1972, *Solar Phys.* **26**, 441.

Brown, J. C.: 1975, in S. R. Kane (ed.), 'Solar Gamma-, X-, and EUV Radiations', *Proc. IAU Symp.* **68**, 305.

Brown, J. C. and Smith, D. F.: 1980, *Rep. Prog. Phys.* **43**, 25.

Brown, J. C., Hayward, J., and Spicer, D. S.: 1981, *Astrophys. J.* **245**, 721.

Brown, J. C., McClymont, A. N., and Mclean, I. S.: 1974, *Nature* **247**, 448.

Brown, J. C., Melrose, D. B., and Spicer, D. S.: 1979, *Astrophys. J.* **228**, 592.

Brown, J. C., Carlaw, V. A., Cronwell, D., and Kane, S. R.: 1983, *Solar Phys.* **88**, 281.

Canfield, R. C., Gunkler, T. A., and Kiplinger, A. L.: 1984, Preprint UCSD, SP-84–19.

Catalano, C. P. and Van Allen, J. A.: 1973, *Astrophys. J.* **185**, 335.

Chubb, T. A.: 1970, in E. R. Dyer (ed.), *Solar Terrestrial Physics*, Part I, D. Reidel Publ. Co., Dordrecht, Holland, p. 99.

Craig, I. J. D., McKinnon, A. L., and Vilmer, N.: 1985, *Solar Phys.* **116**, 377.

Datlowe, D. W., O'Dell, S. L., Peterson, L. E., and Elcan, M. J.: 1977, *Astrophys. J.* **212**, 561.

Davis, J. and Rogerson, J. E.: 1977, *Solar Phys.* **51**, 185.

Dennis, B. R.: 1985, *Solar Phys.* **100**, 465.

Dennis, B. R.: 1988, *Solar Phys.* **118**, 49.

Dermer, C. D. and Ramaty, R.: 1986, *Astrophys. J.* **301**, 962.

Duijveman, A., Hoyng, P., and Machado, M. E.: 1982, *Solar Phys.* **81**, 137.

Elwert, G.: 1939, *Ann. Physik* **34**, 178.
Elwert, G.: 1968, in A. O. Kiepenheuer (ed.), 'Structure and Development of Solar Active Regions', *IAU Symp.* **35**, 444.
Elwert, G. and Haug, E.: 1970, *Solar Phys.* **15**, 234.
Elwert, G. and Haug, E.: 1971, *Solar Phys.* **20**, 413.
Emslie, A. G.: 1983, *Astrophys. J.* **271**, 367.
Fisher, G. H., Canfield, R. C., and McClymont, R. N.: 1985, *Astrophys. J.* **216**, 123.
Gluckstern, R. L. and Hull, M. H.: 1953, *Phys. Rev.* **A90**, 1030.
Haug, E.: 1972, *Solar Phys.* **25**, 425.
Haug, E.: 1979, *Solar Phys.* **61**, 129.
Haug, E., Elwert, G., and Rausaria, R. R.: 1985a, *Astron. Astrophys.* **146**, 159.
Haug, E., Elwert, G., and Rausaria, R. R.: 1985b, *Astron. Astrophys.* **148**, 115.
Henoux, J. C.: 1975, *Solar Phys.* **42**, 219.
Hoyng, P., Brown, J. C., and Van Beek, H. F.: 1976, *Solar Phys.* **48**, 197.
Hoyng, P. *et al.*: 1981, *Astrophys. J.* **246**, L155.
Holt, S. S. and Cline, T. L.: 1968, *Astrophys. J.* **154**, 1027.
Holt, S. S. and Ramaty, R.: 1969, *Solar Phys.* **8**, 119.
Hurley, K., Niel, M., Talon, R., Estulin, I. V., and Dolidze, V. Ch.: 1983, *Astrophys. J.* **265**, 1976.
Kahler, S. W.: 1975, in S. R. Kane (ed.), 'Solar Gamma-, X- and EUV Radiation', *IAU Symp.* **68**, 211.
Kane, S. R.: 1974, in G. Newkirk, Jr. (ed.), 'Coronal Disturbances', *IAU Symp.* **57**, 105.
Kane, S. R. and Anderson, K. A.: 1970, *Astrophys. J.* **162**, 1003.
Kane, S. R. and Donnelly, R. F.: 1971, *Astrophys. J.* **164**, 151.
Kane, S. R., Anderson, K. A., Evans, W. D., Klebesadel, R. W., and Laros, J.: 1979, *Astrophys. J.* **233**, L151.
Kane, S. R., Anderson, K. A., Evans, W. D., Klebesadel, R. W., and Laros, J.: 1980, *Astrophys. J.* **239**, L85.
Kane, S. R., Fenimore, E. E., Klebesadel, R. W., and Laros, J. G.: 1988, *Astrophys. J.* **326**, 1017.
Kane, S. R., Kai, K., Kosugi, T., Enome, S., Landecker, P. B., and McKenzie, D. L.: 1983, *Astrophys. J.* **271**, 376.
Kiplinger, A. L., Dennis, B. R., Emslie, A. G., Frost, K. J., and Orwig, L. E.: 1983a, *Astrophys. J.* **265**, L991.
Kiplinger, A. L., Dennis, B. R., Frost, K. J., and Orwig, L. E.: 1983b, *Astrophys. J.* **273**, 783.
Kiplinger, A. L., Dennis, B. R., Frost, K. J., and Orwig, L. E.: 1984, *Astrophys. J.* **287**, L105.
Korchak, A. A.: 1967, *Soviet Phys. Doklady* **12**, 192.
Koul, P. K., Moza, K. L., Khosa, P. N., and Rausaria, R. R.: 1985, *Astrophys. J.* **292**, 725.
Koul, P. K., Rausaria, R. R., and Khosa, P. N.: 1987, *Solar Phys.* **108**, 139.
Langer, S. H. and Petrosian, V.: 1977, *Astrophys. J.* **215**, 666.
Leach, J. and Petrosian, V.: 1981, *Astrophys. J.* **251**, 781.
Leach, J. and Petrosian, V.: 1983, *Astrophys. J.* **269**, 715.
Lin, R. P., Mewaldt, R. A., and Van Hollebeke, M. A. I.: 1982, *Astrophys. J.* **253**, 949.
Lu, E. T. and Petrosian, V.: 1988, *Astrophys. J.* **327**, 405.
MacKinnon, A. L., Brown, J. C., and Hayward, J.: 1985, *Solar Phys.* **99**, 231.
Nakada, M. P., Neupert, W. M., and Thomas, R. J.: 1974, *Solar Phys.* **37**, 429.
Ohki, K.: 1969, *Solar Phys.* **7**, 260.
Petrosian, V.: 1973, *Astrophys. J.* **186**, 291.
Petrosian, V.: 1985, *Astrophys. J.* **299**, 987.
Pinter, S.: 1969, *Solar Phys.* **8**, 140.
Rieger, E., Reppin, C., Kanbach, G., Forrest, D. J., Chupp, E. L., and Share, G. H.: 1983, *18th Int. Cosmic Ray Conf., Bangalore* **12**, 238.
Sauter, F.: 1934, *Ann. Physik* **20**, 404.
Smith, D. F. and Auer, L. H.: 1980, *Astrophys. J.* **238**, 1126.
Suri, A. N., Chupp, E. L., Forrest, D. F., and Reppin, C.: 1975, *Solar Phys.* **43**, 415.
Švestka, Z.: 1976, *Solar Flares*, D. Reidel Publ. Co., Dordrecht, Holland.
Takakura, T.: 1966, *Space Sci. Rev.* **5**, 80.
Takakura, T., Tanaka, K., Nitta, N., Kai, K., and Ohki, K.: 1986, *Solar Phys.* **107**, 109.
Tanaka, K.: 1987, *Publ. Astron. Soc. Japan* **39**, 1.
Tindo, I. P., Ivanov, V. D., Mandel'stam, S. L., and Shuryghin, A. I.: 1970, *Solar Phys.* **14**, 204.
Tindo, I. P., Ivanov, V. D., Mandel'stam, S. L., and Shuryghin, A. I.: 1972a, *Solar Phys.* **24**, 429.

Tindo, I. P., Ivanov, V. D., Valníček, B., and Lifshits, M. A.: 1972b, *Solar Phys.* **27**, 426.
Tindo, I. P., Shuryghin, A. I., and Steffen, W.: 1976, *Solar Phys.* **46**, 219.
Tramiel, L. J., Chanan, G. A., and Novick, P.: 1984, *Astrophys. J.* **280**, 440.
Tsuneta, S., Takakura, T., Nita, N., Ohki, K., Tanaka, K., Makishime, K., Murakami, T., Oda, M., Ogawara, Y., and Kondo, I.: 1984, *Astrophys. J.* **280**, 887.
Van Beek, H. F., De Feiter, L. D., and de Jager, C.: 1974, *Solar Phys.* **32**, 81.
Vestrand, T., Forrest, J. D., Chupp, E. L., Rieger, E., and Share, G. H.: 1987, *Astrophys. J.* **322**, 1010.